High-phase purity two-dimensional perovskites with 17.3% efficiency enabled by interface engineering of hole transport layer

Siraj Sidhik, Yafei Wang, Wenbin Li, Hao Zhang, Xinjue Zhong, Ayush Agrawal, Ido Hadar, Ioannis Spanopoulos, Anamika Mishra, Boubacar Traore, et al.

To cite this version:

Siraj Sidhik, Yafei Wang, Wenbin Li, Hao Zhang, Xinjue Zhong, et al.. High-phase purity two-dimensional perovskites with 17.3% efficiency enabled by interface engineering of hole transport layer. Cell Reports Physical Science, 2021, 2 (10), pp.100601. 10.1016/j.xcrp.2021.100601 . hal-03371581

HAL Id: hal-03371581
https://hal.science/hal-03371581v1

Submitted on 8 Oct 2021

Cell Reports
Physical Science

CellPress
OPEN ACCESS

Article

High-phase purity two-dimensional perovskites with 17.3% efficiency enabled by interface engineering of hole transport layer

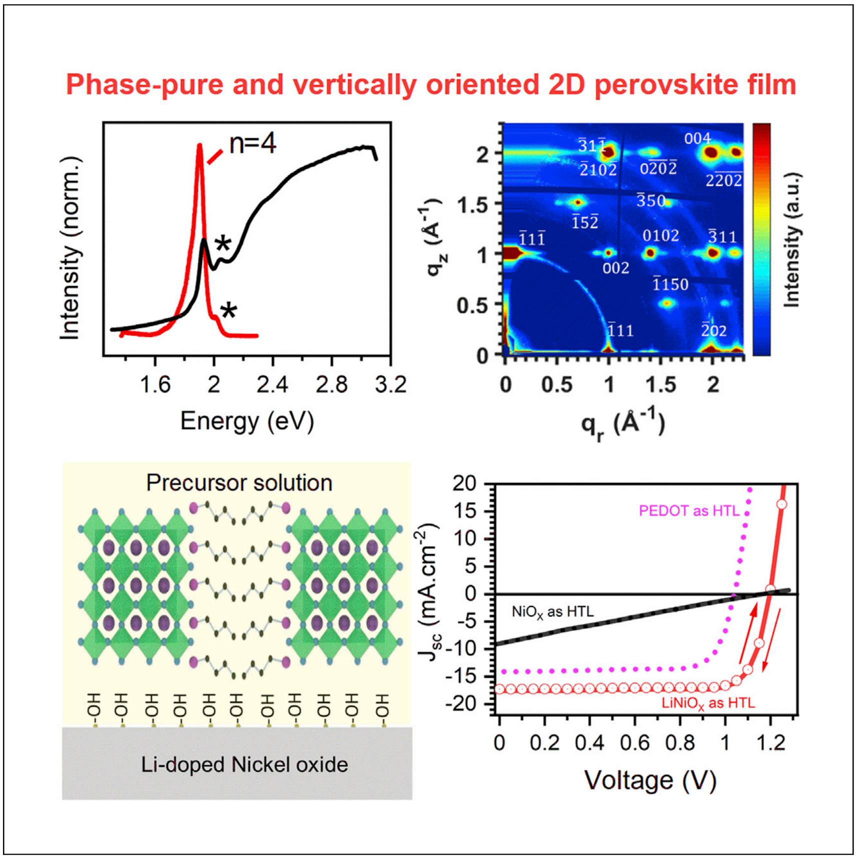

Sidhik et al. report a high-efficiency 2D hybrid perovskite solar cell with an open circuit voltage of 1.22 V by using Li-doped nickel oxide as the hole transport layer with a phase-pure vertically oriented thin film.

Siraj Sidhik, Yafei Wang, Wenbin Li, ..., Antoine Kahn, Mercouri G. Kanatzidis, Aditya D. Mohite

adm4@rice.edu

Highlights

High-phase purity 2D perovskite films with near-perfect vertical orientation

Lithium doped nickel oxide as HTL improves the 2D perovskite film quality

High efficiency of 17.3% enabled by an open circuit voltage of 1.22 V

Enhanced stability with T_{99} = 400 h at 1 sun and T_{90} of 100 h at 5 suns

Sidhik et al., Cell Reports Physical Science *2*, 100601
October 20, 2021 © 2021 The Authors.
https://doi.org/10.1016/j.xcrp.2021.100601

Please cite this article in press as: Sidhik et al., High-phase purity two-dimensional perovskites with 17.3% efficiency enabled by interface engineering of hole transport layer, Cell Reports Physical Science (2021), https://doi.org/10.1016/j.xcrp.2021.100601

Cell Reports
Physical Science

CellPress
OPEN ACCESS

Article

High-phase purity two-dimensional perovskites with 17.3% efficiency enabled by interface engineering of hole transport layer

Siraj Sidhik,[1,2] Yafei Wang,[1] Wenbin Li,[1,3] Hao Zhang,[1,3] Xinjue Zhong,[4] Ayush Agrawal,[1] Ido Hadar,[5] Ioannis Spanopoulos,[5,10] Anamika Mishra,[1,6,7] Boubacar Traoré,[8,9] Mohammad H.K. Samani,[1] Claudine Katan,[9] Amanda B. Marciel,[1] Jean-Christophe Blancon,[1] Jacky Even,[8] Antoine Kahn,[4] Mercouri G. Kanatzidis,[5] and Aditya D. Mohite[1,2,11,*]

SUMMARY

State-of-the-art p-i-n-based 3D perovskite solar cells (PSCs) use nickel oxide (NiO_X) as an efficient hole transport layer (HTL), achieving efficiencies >22%. However, translating this to phase-pure 2D perovskites has been unsuccessful. Here, we report 2D phase-pure Ruddlesden-Popper $BA_2MA_3Pb_4I_{13}$ perovskites with 17.3% efficiency enabled by doping the NiO_X with Li. Our results show that progressively increasing the doping concentration transforms the photoresistor behavior to a typical diode curve, with an increase in the average efficiency from 2.53% to 16.03% with a high open-circuit voltage of 1.22 V. Analysis reveals that Li doping of NiO_X significantly improves the morphology, crystallinity, and orientation of 2D perovskite films and also affords a superior band alignment, facilitating efficient charge extraction. Finally, we demonstrate that 2D PSCs with Li-doped NiO_X exhibit excellent photostability, with T_{99} = 400 h at 1 sun and T_{90} of 100 h at 5 suns measured at relative humidity of 60% ± 5% without the need for external thermal management.

INTRODUCTION

Organic-inorganic hybrid perovskites have gained a great deal of attention in the field of photovoltaics due to the rapid increase in efficiency from 3% to 25%.[1] The state-of-the-art p-i-n based three-dimensional (3D) perovskite solar cells (PSCs) achieve high efficiencies by using a nickel oxide (NiO_X) or lithium (Li)-doped NiO_X hole transport layer (HTL) with high-charge carrier mobility, desired wettability, and enhanced stability.[2–5] However, the 3D perovskites lack long-term intrinsic stability. Several strategies have been implemented to improve stability, including replacing the methylammonium cation with multicomponent cation-based perovskites such as formamidinium, methylammonium, and cesium cation or adding interfacial barrier layers between the perovskite absorber and the transport layers.[6–9] The introduction of 2D Ruddlesden-Popper perovskites with the general formula $(RNH_3)_2A_{n-1}M_nX_{3n+1}$, where RNH_3 represents the bulkier alkyl ammonium cation, A stands for smaller organic or alkyl metal cation, M and X represent the group IVA metal cation and the halogen, and n is an integer that represents the number of the perovskite slabs sandwiched between the bulky ammonium bilayers, indicating the purity of the 2D perovskites.[10–12] Recent work on 2D PSCs has shown that they not only inherit the attractive physical properties of 3D but also possess a

[1]Department of Chemical and Biomolecular Engineering, Rice University, Houston, TX 77005, USA

[2]Department of Materials Science and NanoEngineering, Rice University, Houston, TX 77005, USA

[3]Applied Physics Program, Smalley-Curl Institute, Rice University, Houston, TX 77005, USA

[4]Department of Electrical and Computer Engineering, Princeton University, Princeton, NJ 08544, USA

[5]Department of Chemistry and Department of Materials Science and Engineering, Northwestern University, Evanston, IL 60208, USA

[6]Advanced Materials and Devices Metrology Division, CSIR-National Physical Laboratory, Dr. K.S. Krishnan Marg, New Delhi 110012, India

[7]Academy of Scientific and Innovative Research (AcSIR), Ghaziabad 201002, India

[8]Univ Rennes, INSA Rennes, CNRS, Institut FOTON - UMR 6082, 35000 Rennes, France

[9]Univ Rennes, ENSCR, INSA Rennes, CNRS, ISCR (Institut des Sciences Chimiques de Rennes)–UMR 6226, 35000 Rennes, France

[10]Present address: Department of Chemistry, University of South Florida, Tampa, FL, 33620, USA

[11]Lead contact

*Correspondence: adm4@rice.edu

https://doi.org/10.1016/j.xcrp.2021.100601

superior intrinsic stability.[10,13–15] However, the 2D perovskites still lag in efficiency as compared to their 3D counterpart due to two key limitations. First, despite the near-perfect vertical orientation of the 2D layers, the charge transport is limited by the recombination of carriers at the organic-inorganic interfaces due to the imperfect crystal packing in thin films resulting in field-dependent transport.[13] This places an upper limit on the thickness of the 2D film (~220 nm) resulting in inefficient light absorption in comparison with a 3D perovskite film with >500 nm thickness.[16–18] Second, thin films exhibit heterogeneity in the layer thickness (also known as phase purity or n-value), which has been shown to result in losses in the overall open circuit voltage because the photogenerated charge carrier funnels to the lowest energy level. As a result, the majority of p-i-n-based 2D perovskite photovoltaic devices have been fabricated on PEDOT: PSS (poly 3,4-ethylene dioxythiophene: poly 4-styrene sulfonate), which typically yields an open circuit voltage of 1 V due to the lower ionization energy (IE) of the 2D perovskites and significant interfacial recombinations due to ionic interaction and inferior crystallinity of perovskites on PEDOT.[11,13,19,20] There have also been reports on using alternative organic HTLs, such as poly (triarylamine) (PTAA); however, its hydrophobicity makes wetting of the perovskite solution difficult.[21] Beyond the organic HTLs, there have been very few reports on using inorganic HTLs such as NiO to produce stable 2D PSCs. These devices also show relatively low efficiencies, which were attributed to the increased resistance of 2D perovskites with the NiO_X HTL.[22,23] In addition, these devices used a 2D perovskite thin film with a mixture of 2D and 3D phases, making it challenging to understand the interfacial characteristics between the 2D perovskite and the inorganic HTL.[22,23]

In this work, we show that by using Li-doped NiO_x as an HTL in combination with high-phase purity (~97%) $BA_2MA_3Pb_4I_{13}$ 2D perovskites, we can tailor the film crystallinity, orientation, and energy level alignment to achieve a solar cell with a champion efficiency of 17.3%. The higher efficiency was enabled by a high V_{OC} of 1.22 V resulting from the high-purity 2D perovskite, which lends a homogeneous energy landscape (~97%) with a negligible contribution from impurities (higher n values). External quantum efficiency (EQE) measurements show that the contribution of impure phases is 0.6 mA/cm^2, which is <5% of the total J_{SC}, also consistent with the phase purity obtained from absorbance and X-ray diffraction (XRD) measurements.[12,23] Analysis of the photovoltaic devices revealed that with increasing Li doping concentration in the NiO_x, the behavior transformed from a linear photoresistor (average PCE = 2.53%) to a diode curve (average PCE = 16.03%). Comparison of grazing incidence wide-angle X-ray scattering (GIWAXS) measurements performed on PEDOT: PSS and Li-doped NiO_x revealed a drastic improvement in the morphology and crystallinity, along with a near-perfect vertical orientation of the 2D perovskite thin films grown on Li-doped NiO_x, thereby enabling efficient charge transport and extraction. Photoemission spectroscopy indicated that the Li doping in NiO_x results in a shallower VBM, resulting in a better energy alignment between the VBM of the 2D perovskite and that of the Li-doped NiO_x, which was further validated by observing a 2-fold quenching of the PL signal compared to bare NiO_X substrate. Finally, the use of a stable Li-doped NiO_x HTL further accentuates the stability of 2D perovskites and results in excellent stability with almost no degradation (T_{99} = 400 h) at 1 sun and a T_{90} of 100 h at 5 suns measured at 60% ± 5% relative humidity at maximum power point (MPP) tracking without any external thermal management. These results demonstrate that by combining an appropriate HTL with high-phase purity 2D perovskites, one can realize high-efficiency solar cells without compromising operational stability. We anticipate that this work will lay the foundation for a 2D perovskite photovoltaic technology, with efficiencies that are on par with 3D perovskites but much superior stability.

Please cite this article in press as: Sidhik et al., High-phase purity two-dimensional perovskites with 17.3% efficiency enabled by interface engineering of hole transport layer, Cell Reports Physical Science (2021), https://doi.org/10.1016/j.xcrp.2021.100601

RESULTS AND DISCUSSION

Fabrication and characterization

The NiO_x films were fabricated following a previous report with small modifications,[24] in which the precursors are dissolved in anhydrous ethanol for 3 h for pristine NiO_x and 12 h for Li-doped NiO_x, followed by spin coating on the substrate and sintering at 450°C for 30 min. The 2D perovskite solution of $BA_2MA_3Pb_4I_{13}$ was prepared by dissolving the synthesized high-purity crystals in dimethylformamide (DMF) with 5 wt% methylammonium chloride (MACl) for 6 h at 70°C (Figure S1). Following this, the 2D perovskite films were fabricated by a single-step process detailed in the Method details.

Figure 1 describes the surface chemistry, thin-film morphology, and spectroscopic characteristics of the fabricated NiO_x HTLs and the 2D perovskite, $BA_2MA_3Pb_4I_{13}$. The surface energy of the underlying NiO_x HTL plays a major role in controlling the morphology of 2D perovskite film. Contact angle measurements were performed by drop casting the 2D perovskite solution onto the Li-doped and pristine NiO_x surfaces. The Li-doped NiO_x showed enhanced wettability compared to the pristine NiO_x film (Figures 1A and 1B). This indicates that the introduction of Li in the NiO_x HTL increases the surface energy of the NiO_x substrate and leads to improved interfacial properties of the 2D perovskite film, which is studied in detail using the X-ray photoelectron spectroscopy (XPS) measurements. The Ni $2p_{3/2}$ spectra of the NiO_X and Li-doped NiO_X are presented in Figures 1C and 1D. The deconvolution of the Ni $2p_{3/2}$ binding energies in the NiO_x can be fitted to NiO (Ni^{2+}, 853.4 eV), Ni_2O_3 (Ni^{3+}, 855.7 eV), and a shake-up satellite peak (861.02 eV). The Li-doped NiO_x shows an additional peak of $Ni(OH)_2$ (856.8 eV) attributed to the adsorption of H_2O due to the presence of Li in the film.[25] The ratio of the integrated area of the Ni^{2+}/Ni^{3+}bonding states was observed to increase from 0.6 to 1.05 with the introduction of Li in the NiO_X, resulting in an improved conductivity.[26–29] The O 1 s XPS spectra are depicted in Figure S2. The deconvolution of the O 1 s peaks can be fitted to the lattice oxygen (529.38 eV) and oxygen vacancies (531.38 eV).[30] With the introduction of Li in the NiO_X, we observed an additional peak at 530.3 eV, which can be assigned to the interaction of Li with the oxygen (Li-O).[26,28] In addition, the Li-doped NiO_X consists of adsorbed O or H_2O (533.0 eV) on the surface. The presence of these –OH groups on the surface of Li-doped NiO_X makes it superhydrophilic, which is also verified by the contact angle measurements (see Figure 1B). In addition, we observed a slight increase in the O vacancies, which may be due to the intercalation of Li in the NiO_X lattice.[25,27] Furthermore, to visualize the morphological characteristics of the fabricated films, we performed atomic force microscopy (AFM) and scanning electron microscopy (SEM) measurements. The root-mean-square (RMS) roughness of the NiO_x surface increased from 5.3 to 6.3 nm, with a slight increment in the grain size, following the introduction of Li (Figure S3). After depositing the 2D perovskite film on top of both the NiO_X surfaces, we measured the cross-sectional SEM image, which indicates similar thicknesses of the 2D perovskite film (~200–250 nm) (Figures 1E and 1F). The 2D perovskite films grown on top of the Li-doped NiO_X surfaces appear to be bulk-like, with few grain boundaries. In contrast, films on the pristine NiO_x surface nucleate with several significantly large densities of grain boundaries and non-uniform cross-sections, which were also confirmed by the surface SEM and AFM measurements (Figures 1G, 1H, and S4). We obtained an ultra-smooth film on top of Li-doped NiO_X (RMS roughness = 3.9 nm) as compared to the one grown on pristine NiO_x (RMS roughness = 8.3 nm), enabled by the superhydrophilic nature of the Li-doped NiO_x substrate increasing the adhesion with the perovskite solution.[31–34] The optical

Please cite this article in press as: Sidhik et al., High-phase purity two-dimensional perovskites with 17.3% efficiency enabled by interface engineering of hole transport layer, Cell Reports Physical Science (2021), https://doi.org/10.1016/j.xcrp.2021.100601

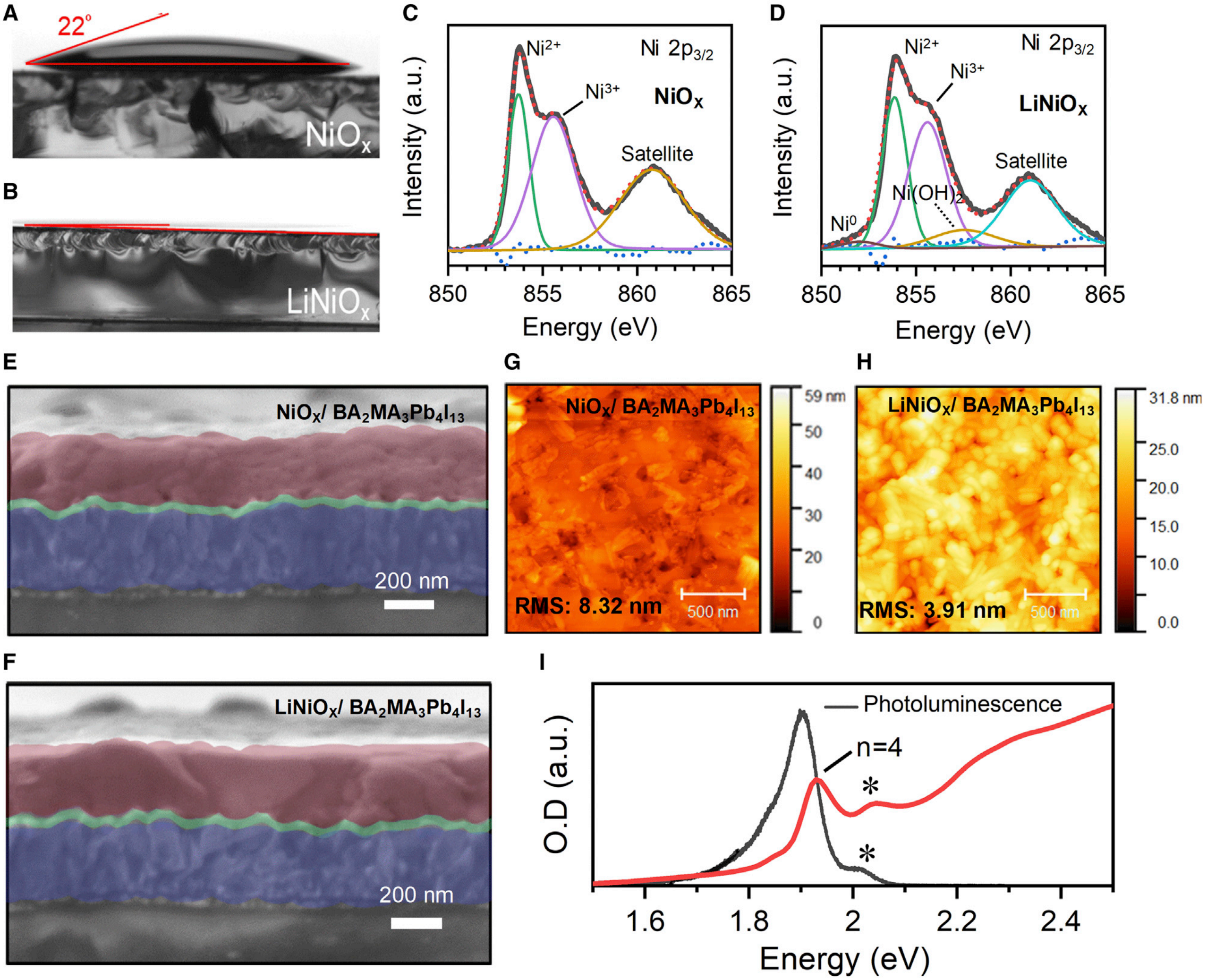

Figure 1. Morphological and spectroscopic characteristics of the 2D perovskite film on NiO$_x$

(A and B) Contact angle measurement showing wettability of (A) pristine NiO$_X$ surface and (B) Li-doped NiO$_X$ surface.

(C and D) Deconvolution of the Ni 2p$_{3/2}$ spectra of the NiO$_X$ and Li-doped NiO$_X$ films indicating the Gaussian fitted peaks of different oxidation states of Ni. The dotted red line indicates the fitted Ni 2p$_{3/2}$ spectra, and the dotted blue line denotes the residual spectra.

(E and F) Cross-sectional scanning electron microscopy image of the 2D perovskite films grown on top of the NiO$_X$ (E) and (F) the LiNiO$_X$ surface, indicating the variation in morphology.

(G and H) Atomic force microscopy image of the fabricated BA$_2$MA$_3$Pb$_4$I$_{13}$ 2D perovskite film on the NiO$_X$- and Li-doped NiO$_X$ surface for evaluating the root-mean-square roughness.

(I) Absorption characteristics of the BA$_2$MA$_3$Pb$_4$I$_{13}$ 2D perovskite film. The star symbol represents the n = 3 impurity peak in the film. No notable variation in the absorption was observed in the 2 samples under study.

absorbance characteristics of BA$_2$MA$_3$Pb$_4$I$_{13}$ 2D perovskite thin-film fabricated on both the NiO$_x$ substrate showed no clear distinction and are depicted in Figure 2I. We directly compared the absorption spectra of 2D perovskite thin films with the 2D perovskite crystals of BA$_2$MA$_3$Pb$_4$I$_{13}$ (see Figure S5), which shows a dominant n = 4 phase with a small n = 3 impurity and negligible higher-order impurities. The percentage of phase purity was evaluated by normalizing the thin film absorption with its absorption coefficient reported by Song et al.,[35] and was found to be ~97% (Figure S6). The photoluminescence (PL) spectra indicate a strong peak at 1.92 eV (644 nm) corresponding to the excitonic absorption of n = 4 phase, with a small shoulder (~2.02 eV) indicating n = 3 phase impurity. The degree of phase

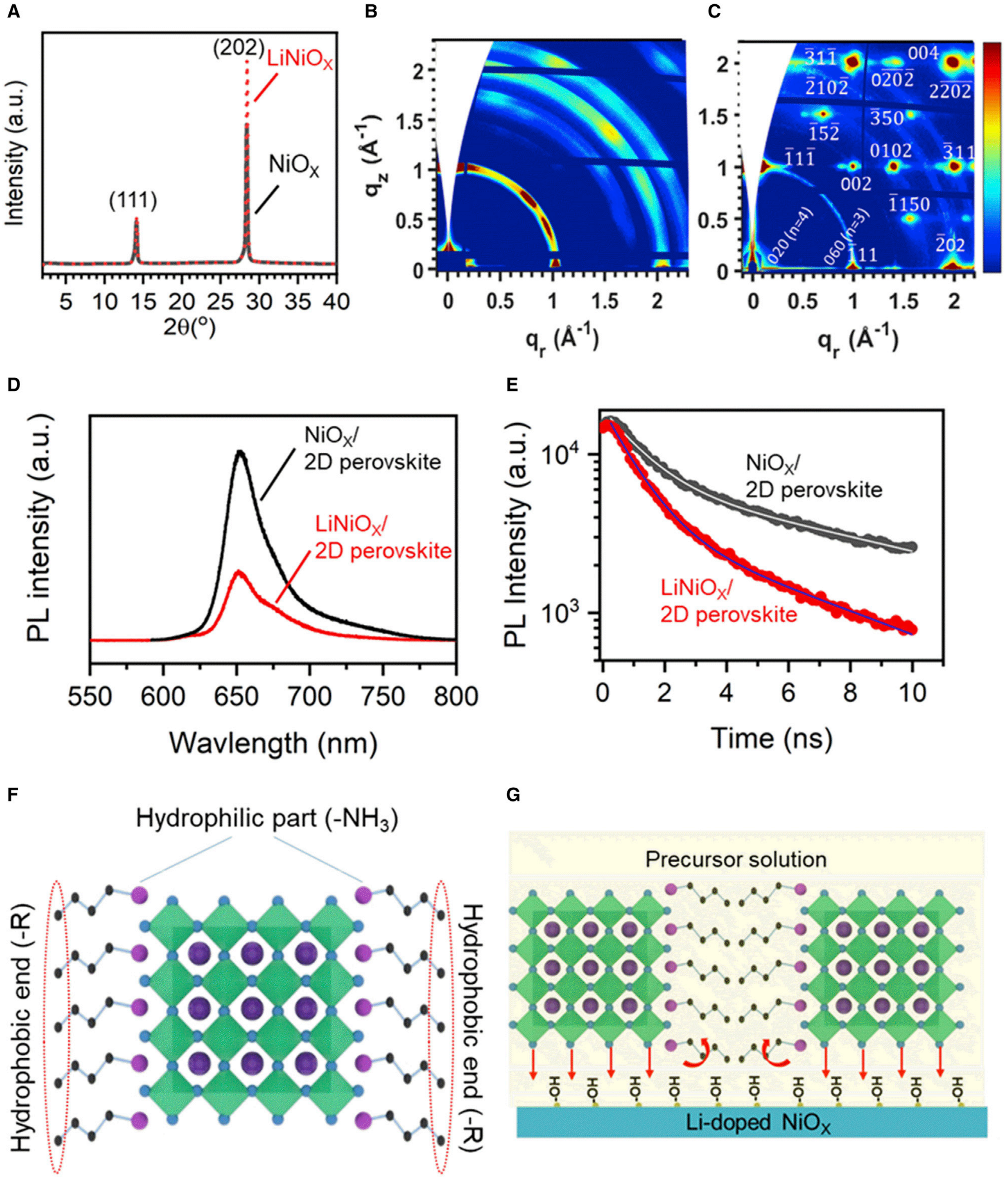

Figure 2. Orientation and interfacial characteristics of 2D perovskite on NiOx surfaces

(A) Grazing incidence X-ray diffraction measurement of the $BA_2MA_3Pb_4I_{13}$ perovskite film grown on the 2 surfaces under investigation showing the variation in orientation.

(B and C) GIWAXS 2D diffraction pattern of the $BA_2MA_3Pb_4I_{13}$ 2D perovskite film fabricated on the pristine NiO_X-doped (B) and (C) the Li-doped NiO_X.

purity was further confirmed by abrasing the thin films and measuring the XRD pattern of the powder (see Figure S7). To understand the mechanism that leads to high-phase purity 2D perovskite, we performed *in situ* XRD measurement on the thin films during their growth, as illustrated in Figure S8.

This was performed by spin coating the 2D perovskite $BA_2MA_3Pb_4I_{13}$ precursor solution on a glass slide, which was kept at room temperature without annealing to slow down the kinetics of nucleation and film formation. The evolution of the XRD pattern was monitored for 80 min immediately after spin coating. The diffraction peaks corresponding to different phases of 2D perovskite were identified and monitored as a function of time. We observed a peak at $q = 1$ Å^{-1} after 1 min, indicating the formation of a perovskite phase, after which the 2D perovskite peaks start evolving. After a few minutes, the n = 3 phase forms rapidly and over time transforms into the thermodynamically stable n = 4 phase (ΔG transformation of n = 3 to n = 4 is negative) by using the existing or unused precursor solution,[36] which can be verified by the increase in peak intensity of the n = 4 phase, following a decrease in the n = 3 phase. This method bypasses the intermediate gel stage, which is usually observed in all of the perovskite film formation techniques, hence avoiding broad phase distribution.[16,17,37]

The crystallinity of the 2D perovskite films was analyzed using grazing incidence X-ray diffraction (GIXRD) (Figure 2A). We observed two dominant diffraction peaks at 14.16° and 28.38° corresponding to the (111) and (202) planes. The full width at half-maximum (FWHM) of the (202) plane reduced from 0.26 for the pristine NiO_X to 0.22 for Li-doped NiO_x, indicating an increase in the correlation length and thus an enhancement in crystallinity of the perovskite film grown on top of the Li-doped NiO_X HTL. We also observed a preferential orientation in the (101) plane confirmed by the increased intensity of the (202) diffraction peak with respect to the (111) peak. The considerable variation observed in the orientation of the 2D perovskite film between the pristine and Li-doped NiO_x HTLs motivated an in-depth 2D crystallographic measurement using GIWAXS presented in Figures 2B and 2C. The GIWAXS pattern was analyzed and indexed depicting the presence of n = 3 and n = 4 phases with a negligible amount of higher-order n-values in the film, matching well with the absorption spectra. However, the two scattering patterns showed a striking difference in orientation. The 2D perovskite film fabricated on the pristine NiO_X exhibited halo rings, which depict the random orientation of the 2D perovskite slabs within the grains of the polycrystalline film (Figure 2B). In contrast, the films grown on top of Li-doped NiO_X showed near-circular discrete Bragg spots along the same ring, indicating preferential orientation (Figure 2C). Moreover, the presence of prominent (111) and (202) reflections in the q_r direction indicate a strongly preferred vertical orientation.[13] An azimuthal angle-dependent intensity integration of the GIWAXS for the (111) diffraction peak ($q = 1.0$ Å^{-1}) corroborates the strong preferred orientation of the 2D film on the Li-doped NiO_x HTL compared to the pristine HTL (Figure S9). The reduction in the FWHM and mosaicity evaluated from the angular profile of the (111) diffraction peak (in the Li-doped NiO_X 2D film) is associated with an increase in correlation lengths as shown by the GIXRD measurements (Figures S9 and S10). To further verify the quality of the 2D perovskite

---

(D) Photoluminescence measurement to probe the bulk of the 2D perovskite film grown on the 2 NiO_x surfaces to evaluate the charge transfer phenomenon.

(E) The time-resolved photoluminescence spectra of the 2D perovskite film grown on top of the 2 NiO_x surfaces to extract the charge carrier lifetime to elucidate the charge transfer to the HTL.

(F) Schematic representation of $BA_2MA_3Pb_4I_{13}$ molecular seed with PbI_2 octahedra and the butylammonium molecule.

(G) Schematic showing the orientation of the $BA_2MA_3Pb_4I_{13}$ film on the Li-doped NiO_X substrate.

film and elucidate the charge transfer mechanism in both films, we performed a series of PL and time-resolved PL measurements. The PL intensity measured for both the 2D perovskite films (without the electron transport layer and the metal contact) is presented in Figure S11A. The PL peak observed at 750 nm corresponds to the edge states or lower energy states, which were probed at a lower fluence of 1 sun ($100\ \mathrm{mW} \cdot \mathrm{cm}^{-2}$).[14,38] At lower fluences, all of the excitons primarily decay by populating the lower energy states. It has been reported that the lower energy states are surface localized in vertically oriented films, while they are distributed in the bulk of the film in a randomly oriented film.[38] The $BA_2MA_3Pb_4I_{13}$ 2D perovskite film fabricated on top of Li-doped NiO_X yields much stronger PL intensity as the excitons can diffuse to the surface and efficiently transfer their energy in a near-single crystalline out-of-plane oriented film. Our recent result shows the exciton diffusion length of 100 nm in a near-single crystalline vertically oriented film.[39] In contrast, the film on top of bare NiO_X, shows a more random orientation giving lower PL emission intensity, presumably due to non-radiative recombination resulting from exciton dissociation at the organic-inorganic interfaces distributed in the film. Hence, this PL measurement probes the quality of the 2D perovskite surface that is used for charge dissociation in optoelectronic devices. Also, the redshift in the PL can be caused by the larger grain size verified by the morphological characterization.[39–41] Furthermore, we performed time-resolved PL (TRPL) measurements to quantify the carrier lifetime of these edge states in both films (Figure S11B). The obtained TRPL curves are fitted with a tri-exponential decay model to extract the carrier lifetime. Table S1 presents the fitted parameters of the tri-exponential fit of the TRPL decay, in which τ_1, and τ_2 correspond to two types of trap-assisted recombination, and τ_3 is ascribed to the radiative recombination process in the perovskite grains. We observed a significant increase in the average carrier lifetime from 2.72 to 19.72 ns for the 2D perovskite films grown on top of Li-doped NiO_X HTL, indicating a reduction in non-radiative recombination on the 2D perovskite surface.

We further increased the fluence to probe the dominant $n = 4$ phase in the $BA_2MA_3Pb_4I_{13}$ 2D perovskite film. The PL consists of a dominant $n = 4$ phase (~653 nm), small $n = 3$ impurity (~620 nm), and a decaying tail in the near-infrared region (NIR), which can be assigned to edge states or higher-order states (see Figure 4D). We observed a significant quenching in the PL intensity of the $BA_2MA_3Pb_4I_{13}$ 2D perovskite fabricated on Li-doped NiO_X when compared to the bare NiO_X as HTL. This phenomenon indicates an efficient charge transfer from the bulk of the 2D perovskite to the Li-doped NiO_X caused due to the reduced surface charge trapping. The time-resolved PL measurements were conducted with an excitation wavelength of 500 nm. Table S2 summarizes the fitting parameters of the TRPL decay for both samples. The Li-doped $NiO_X/BA_2MA_3Pb_4I_{13}$ sample shows a decay time of 6.97 ns, whereas the $NiO_X/BA_2MA_3Pb_4I_{13}$ sample showed a longer decay time of 16.29 ns, indicating that the Li-doped NiO_X has faster and more efficient hole extraction capabilities than the bare NiO_X, which significantly increases the current density and fill factor (FF) of the solar cells[42–44] (see Figure 4E).

The remarkable change in the morphology, crystallinity, and orientation of the 2D perovskite film can be attributed to the strongly hydrophilic nature of the Li-doped NiO_X caused by the hydroxyl (–OH) groups present on the surface. Similar results were reported by Kim et al.[45] for the $MAPbI_3$ film, in which they intentionally introduce the –OH groups on the NiO_X substrates to make the film hydrophilic. The reduced Gibbs free energy for hydrophilic surface results in several nucleation centers, owing to accelerated nucleation kinetics and grain boundary formations.[46–48] At this point in our single-step deposition (immediately after spin coating), the

Please cite this article in press as: Sidhik et al., High-phase purity two-dimensional perovskites with 17.3% efficiency enabled by interface engineering of hole transport layer, Cell Reports Physical Science (2021), https://doi.org/10.1016/j.xcrp.2021.100601

perovskite grains will be small but densely packed. As we are not using an antisolvent method or a hot casting approach, the light-brown 2D perovskite film contains residual DMF. As a result, upon thermal annealing, the perovskite grains further redissolve and coalesce together to form large grains with enhanced crystallinity, similar to the Ostwald ripening process observed in the post-annealing treatment by isopropyl alcohol.[27,49] However, a relatively less hydrophilic surface leads to few nucleation centers,[45] and the perovskite grains are not packed enough to grow into a larger grain during the annealing process as verified by the AFM and SEM images (see Figures 1G, 1H, and S4).

The preferential out-of-plane orientation observed on the Li-doped NiO_X substrate was attributed to the presence of –OH groups on the surface. In a 2D perovskite, the polar ($-NH_3$) group is attached to the lead iodide slabs and the hydrophobic alkyl groups protrude out (see Figure 2F). As a result, when a solution containing the 2D perovskite slabs is introduced on a superhydrophilic Li-doped NiO_X, the PbI_2 octahedra have more affinity to bind on the surface, while the hydrophobic long alkyl chain tries to stay well inside the solution, inducing an out-of-plane orientation[50] (see Figure 2G). This mechanism was also verified for lower n values ($n < 4$), which have a natural tendency to orient horizontally (along the stacking axis).[16] We could achieve a preferential vertical orientation depicted by strong (111), (202) peaks and the missing low-angle peaks (see Figure S12). Hence, in a single-step deposition technique, a hydrophilic surface leads to the formation of dense, compact, crystalline, and oriented 2D perovskite films.

Device evaluation

Considering the drastic change in morphological, orientation, and interfacial characteristics of the 2D perovskite film fabricated on Li-doped NiO_X, we fabricated a p-i-n junction photovoltaic device, FTO/NiO_X/$BA_2MA_3Pb_4I_{13}$/PCBM/Ag with varying doping levels of Li. The fabricated devices with pristine NiO_X as the HTL exhibited a highly resistive behavior under light, having an average efficiency of 2.5% ± 0.5% corresponding to a FF of 27.32% ± 1.0% (Figures 3A, 3B, and S13). We also tested the hot casting approach for growing 2D perovskite film on the pristine NiO_X, which also resulted in a resistive J-V characteristic (Figure S14). Furthermore, we fabricated a series of 2D PSCs with Li-doped NiO_X as the HTL. Figure 3A depicts the variation in the power conversion efficiency (PCE) of the 2D PSCs with varying doping levels of Li salt from 0 mol% to 10 mol%. A large improvement in the average device performance from ~2.53% to ~16.03% was observed with an increase in the doping concentration (0 to 10 mol%), with the greatest improvements observed in the FF and the current density (J_{SC}) (Figure S13). The corresponding J-V characteristics are depicted in Figure 3B. The champion device with Li-doped NiO_X (10 mol% Li doping) as the HTL exhibited a PCE of ~17.3% ($J_{SC} = 17.04\ mA \cdot cm^{-2}$, $V_{OC} = 1.22\ V$, and FF = 83%) corresponding to a major increase in the FF and the J_{SC} (Figures 3C and S9C). These devices showed negligible hysteresis verified by the J-V characteristics measured under different scan directions and scan speeds (Figures 3C and S15). The champion PEDOT: PSS device gave an efficiency of 13.2% corresponding to a V_{OC} of 1.05 V and FF of 77.0%. The considerable increase in V_{OC} observed for the NiO_X-based 2D PSCs can be attributed to improved band-level alignments. The EQE of the best device is presented in Figure 3D. The average EQE is in good agreement with the J_{SC} extracted from the J-V characteristics, with a <5% difference arising from a slight spectral mismatch between the two sources. In addition, the EQE shows a small photogeneration in the NIR below the band gap of n = 4 2D perovskite of 1.85 eV. This corresponded to a current density of $1\ mA \cdot cm^{-2}$ arising from the impurities within the film, which is merely 5.6% of the total J_{SC} of $17.04\ mA/cm^2$.

Please cite this article in press as: Sidhik et al., High-phase purity two-dimensional perovskites with 17.3% efficiency enabled by interface engineering of hole transport layer, Cell Reports Physical Science (2021), https://doi.org/10.1016/j.xcrp.2021.100601

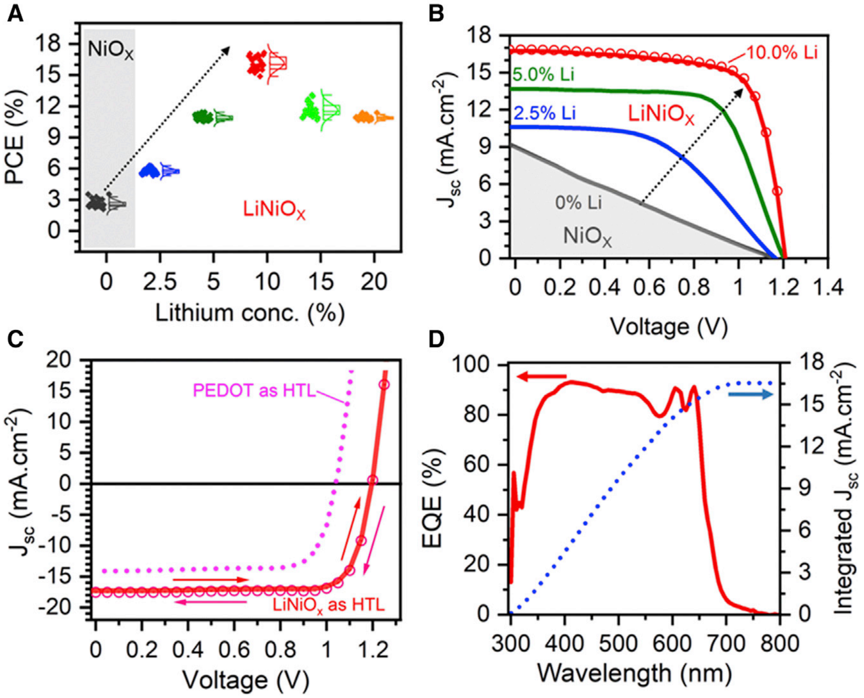

Figure 3. Photovoltaic characteristics of the 2D perovskite solar cell with the NiO$_x$ HTL

(A) The statistics showing the change in the power conversion efficiency of the 2D perovskite solar cell fabricated on NiO$_x$ with varying levels of Li doping.

(B) J-V characteristics of the fabricated 2D perovskite device with varying levels of Li doping.

(C) J-V characteristics of the champion device fabricated on Li-doped NiO$_X$ and PEDOT: PSS as an organic HTL. The arrows indicate the scanning direction, and the characteristics exhibit negligible hysteresis behavior.

(D) The external quantum efficiency (EQE) of the champion 2D perovskite device fabricated on top of Li-doped NiO$_X$.

To further understand the substantial increase in PCE, we studied the electronic characteristics of the NiO$_X$ and Li-doped NiO$_X$ HTLs using correlated optical and electronic measurements. This enables the evaluation of the relative change in conductance and measurement of the variation in band levels in the device architecture. We measured the *I-V* characteristics of the NiO$_x$ films (with varying concentrations of Li-doping) spin coated on top of the fluorine-doped tin oxide (FTO) and sintered, with a top metal contact (Ag). Compared to the pristine NiO$_x$, we observed an increase in conductance (more than a factor of 2) with the introduction of 10% Li (Figure 4A). Upon further increase in the doping (15, 20 mol%), the conductance is substantially reduced, indicating that the excess Li$^+$ may act as scattering centers for charges. Figure S16 shows the *Tauc* plot calculated from the absorbance of the corresponding films, where we observed a reduction in band gap from 3.7 to 3.6 eV with the introduction of 10% Li in the NiO$_X$ film. The Li-induced change in energy of the NiO$_x$ VBM with respect to the vacuum level (i.e., the IE) was measured using ambient photoemission yield spectroscopy (PYS; see Method details). Ultra-high vacuum measurements using ultraviolet (UV) photoemission spectroscopy (UPS) were also performed. The NiO$_x$ IE was observed to decrease from 5.22 to 5.10 eV with ambient photoemission and from 5.0 to 4.8 eV with UPS upon Li doping (Figure 4B). This result is consistent with our previous theoretical prediction indicating that Li doping pushes NiO$_x$ states to a better band-level alignment with the perovskite states at the VBM.[51] Most important, we observed a shift of the NiO$_x$ Fermi level toward the VBM by ~0.18

Please cite this article in press as: Sidhik et al., High-phase purity two-dimensional perovskites with 17.3% efficiency enabled by interface engineering of hole transport layer, Cell Reports Physical Science (2021), https://doi.org/10.1016/j.xcrp.2021.100601

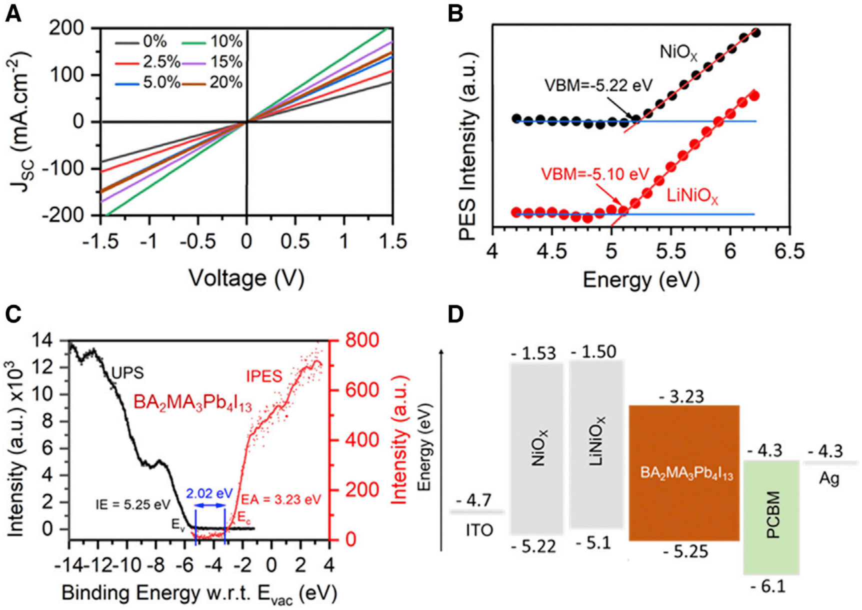

Figure 4. Electronic characteristics of 2D perovskite solar cell with pristine and Li-doped NiO$_x$

(A) Current-voltage characteristics of the NiO$_x$ film, with varying doped Li levels indicating an increase in conductance verified by the change in the slope of the curve.

(B) Plot showing the variation in the position of the valence band maximum (VBM) with respect to the vacuum level (i.e., ionization energy [IE]) of the 2 NiO$_x$ surfaces obtained by photoemission yield spectroscopy (PYS).

(C) Plots showing the determinations of the electron affinity (EA) by inverse photoemission spectroscopy (IPES) and the extracted VBM w.r.t. the vacuum level (i.e., IE) by ultraviolet photoemission spectroscopy (UPS) of the high purity BA$_2$MA$_3$Pb$_4$I$_{13}$ 2D perovskite film. The Fermi level reference for both UPS and IPES was determined on a clean Au surface.

(D) Band diagram of the solar cell assumed from measured energy levels and work functions of various constituents, showing probable charge extraction paths.

eV, from 0.78 eV in the pristine NiO$_X$ film to ~0.6 eV in the Li-doped NiO$_X$ film, consistent with the rise in NiO$_x$ conductance (Figure 4A) due to increased p-type doping achieved by Li incorporation (see Figure S17). Furthermore, we extracted the VBM with respect to the vacuum level (i.e., IE of the high-purity BA$_2$MA$_3$Pb$_4$I$_{13}$ 2D perovskite film using the UPS), and the electron affinity (EA) using the inverse photoemission spectroscopy (IPES) (Figures 4C and S18). The Fermi level reference for these combined UPS and IPES experiments was determined on a clean Au surface. Using these results, an energy diagram representing the solar cell architecture with the band energies evaluated is presented in Figure 4D. As one cannot measure energy-level alignment at buried interfaces, the diagram provides a view of the device's electronic structure assuming vacuum-level alignment at each interface. Nevertheless, we observe an appropriate step-like VBM alignment for the Li-doped NiO$_X$ to the BA$_2$MA$_3$Pb$_4$I$_{13}$ 2D perovskite for efficient hole extraction through the doped, more conductive HTL, which helps in fabricating highly efficient photovoltaic devices.[51]

Finally, to evaluate the photostability of the device, we performed measurements under continuous light soaking with the air mass 1.5 global (AM 1.5G) filter for the 2D PSCs with Li-doped NiO$_X$. We recorded the variation in PCE at the MPP as a function of illumination time and light power, as illustrated in Figure 5. The devices were encapsulated using UV-curable epoxy and measured under 60% ± 5%

Please cite this article in press as: Sidhik et al., High-phase purity two-dimensional perovskites with 17.3% efficiency enabled by interface engineering of hole transport layer, Cell Reports Physical Science (2021), https://doi.org/10.1016/j.xcrp.2021.100601

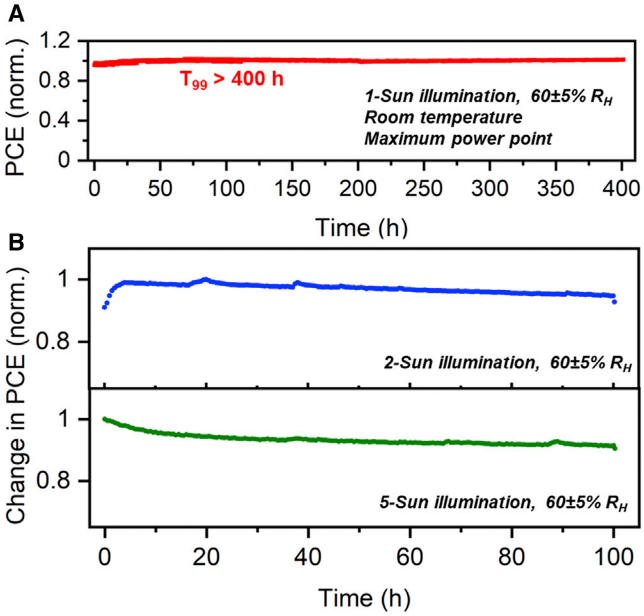

Figure 5. Photostability of 2D perovskite photovoltaic devices

(A) Photostability of 2D perovskite photovoltaic devices under continuous 1 sun (100 mW · cm^{-2}) illumination measured on an encapsulated device at a relative humidity of 60% ± 5%.

(B) Photocurrent stability as a function of illumination time and incident power (2- and 5-sun) measured on an encapsulated device at a humidity of 60% ± 5%.

relative humidity in the air. The device exhibits excellent stability under constant 1 sun illumination without additional UV filters showing <99% degradation for 400 h (Figure 5A). We further performed an accelerated test by monitoring the change in PCE under higher light intensities (2 and 5 suns illumination), as shown in Figure 5B. The devices exhibit a stable output for up to 5 suns illumination during the testing period. The degradation starts after several hours of light soaking for the higher intensities, most likely due to the increase in temperature of the device, which could be avoided by convective cooling of the devices. The enhanced photostability shown by the device is an indication of high-quality 2D perovskite film and its interface.

In summary, we showed a state-of-the-art Li-doped NiO_x-based $BA_2MA_3Pb_4I_{13}$ 2D PSC with a champion efficiency of 17.3%. The photovoltaic device with the pristine NiO_X showed a highly resistive behavior under light (average PCE = 2.53%), which was significantly improved with the introduction of Li (average PCE = 16.03%). The presence of Li in the NiO_x films not only improved the morphology and crystallinity of the 2D perovskite films but also altered the orientation of the 2D perovskite crystallite domains drastically. The preferred orientation has a beneficial effect on the reduction of non-radiative recombinations, leading to efficient charge carrier separation and transport. The electronic studies predicted the presence of a hole-extraction barrier between the 2D perovskite and pristine NiO_x, which was significantly reduced with the introduction of Li. In addition, we observed enhanced p-type doping in the Li-doped NiO_X, which increased the conductance of the layer significantly. The devices also showed enhanced photostability under rigorous testing conditions. This work could open up the field of 2D perovskites by providing an efficient HTL with low photovoltage losses and enhanced charge transfer characteristics. In addition, this could also provide a deeper understanding of the interface

Please cite this article in press as: Sidhik et al., High-phase purity two-dimensional perovskites with 17.3% efficiency enabled by interface engineering of hole transport layer, Cell Reports Physical Science (2021), https://doi.org/10.1016/j.xcrp.2021.100601

between a pure 2D perovskite film and metal-oxide-based transport layers, which have never been studied.

EXPERIMENTAL PROCEDURES

Resource availability

Lead contact

Further information and requests for resources and reagents should be directed to and will be fulfilled by the lead contact, Aditya D. Mohite (adm4@rice.edu).

Materials availability

This study did not generate new unique reagents.

Data and code availability

All data related to this study included in the article and Supplemental information will be provided by the lead contact upon reasonable request.

NiO_X solution preparation

The NiO_X solution was prepared by dissolving 0.1 M nickel acetate tetrahydrate and monoethanolamine (1:1) in anhydrous ethanol. The solution was left on the hot plate stirring at 70°C for 3 h. For preparing the Li-doped NiO_X solution, lithium nitrate at different mol% (2.5, 5, 10, 15, and 20) was added to the solution and left stirring at 70°C for >12 h.

2D $BA_2MA_3Pb_4I_{13}$ perovskite solution preparation

The perovskite solution was prepared by dissolving the synthesized 2D perovskite crystal powders of $BA_2MA_3Pb_4I_{13}$ in *N*,*N*-DMF with an additive of 5.0 wt% of MACl. The solution was aged on a hot plate at 70°C without stirring for 6 h.

Solar cell fabrication

The patterned FTO substrates were cleaned by sonicating in soap water, water, acetone, ethanol, and acetone (1:1) for 15 min each. The substrates were further dried under flowing N_2 and left under UV for 30 min. The NiO_X and Li-doped NiO_X solutions were immediately spin coated on the FTO at 5,000 rpm for 30 s, followed by 3-step annealing, 150°C for 10 min, 300°C for 15 min, and finally 450°C for 30 min. The entire fabrication process was carried out in ambient air. The sintering process at 450°C is critical for producing a highly reproducible Li-doped NiO_X film. The substrates were transferred to the Ar-filled glove box for the rest of the device fabrication process. The 2D perovskite solution was spin coated at 4,000 rpm for 30 s, followed by annealing at 100°C for 10 min. Furthermore, the PCBM solution (25 mg/mL) in chlorobenzene was spin coated at 1,000 rpm for 45 s, followed by thermal evaporation of 1 nm bathocuproine and then 100 nm Ag as the metal contact.

Ambient photoemission measurement

The VBM energy of NiO_X and Li-doped NiO_X films was measured by PES in the air (PYSA, AC-2, Riken-Keiki). Briefly, the sample is scanned by tunable monochromatic UV light (4.2–6.2 eV), under ambient conditions, and the number of generated photoelectrons is measured at each excitation energy. Photoelectrons are only generated when the photon energy is higher than the ionization energy. The VBM is determined by finding the onset of the PYSA spectra.

UV photoemission spectroscopy measurements

The UPS measurements were performed in ultrahigh vacuum (10^{-10} torr) at room temperature. HeI (21.22 eV) photons generated by a discharged lamp were used to probe the work function (WF) and valence band edges. Valence band spectra were recorded and plotted on a logarithmic intensity scale due to the low density of states near the band edge. The ionization energy of the material is determined by combining the WF and valence band edge with respect to the Fermi level.

Solar cell characterization

The solar cells were characterized by taking current-voltage curves under a solar simulator with a light intensity equivalent to 1 sun (100 mW · cm^{-2}) with the air mass 1.5 G filter. The devices were covered with appropriate masks to reduce the error due to the edges. The EQE was measured by illuminating the active area of the device using the monochromatic light using a tungsten source (chopped at 150 Hz) while collecting the photocurrent by a lock-in amplifier in AC mode. The light source spectrum response was corrected by calibrated silicon diode (FDS1010, Thorlabs).

SUPPLEMENTAL INFORMATION

Supplemental information can be found online at https://doi.org/10.1016/j.xcrp.2021.100601.

ACKNOWLEDGMENTS

A.D.M. acknowledges research support from the HydroGEN Advanced Water Splitting Materials Consortium, established as part of the Energy Materials Network under the U.S. Department of Energy, Office of Energy Efficiency and Renewable Energy, Hydrogen and Fuel Cell Technologies Office, under the Award Number DE-EE0008843. J.E. acknowledges the financial support from the Institut Universitaire de France. At Northwestern, this work was supported by the Office of Naval Research (ONR) under grant no. N00014-20-1-2725. A.B.M. acknowledges financial support from The Welch Foundation (C-2003-20190330) and Rice University. This research used facilities of the Advanced Photon Source, a US Department of Energy (DOE) Office of Science User Facility operated for the DOE Office of Science by Argonne National Laboratory under contract no. DE-AC02-06CH11357. This research used the beamline 11-BM of the National Synchrotron Light Source II, a DOE Office of Science user facility operated for the DOE Office of Science by Brookhaven National Laboratory under contract no. DE-SC0012704. Work at Princeton University was supported by agrant from the US-Israel Binational Science Foundation (BSF Grant No. 2018349). B.T. and C.K. acknowledge funding from the European Union's Horizon 2020 program, through an Innovation Action under the grant agreement No. 861985 (PeroCUBE).

AUTHOR CONTRIBUTIONS

Conceptualization, S.S., Y.W., and A.D.M.; methodology, S.S., W.L., H.Z., X.Z., I.H., and I.S.; investigation, S.S. and Y.W.; formal analysis, S.S. and W.L.; writing – original draft, S.S. and A.D.M.; writing – review & editing, C.K., J.E., J.-C.B., A.B.M., A.K., M.G.K., A.A., B.T., M.H.K.S., and A.D.M.; supervision, J.E., M.G.K., and A.D.M.

DECLARATION OF INTERESTS

The authors declare no competing interests.

Received: May 6, 2021
Revised: August 25, 2021
Accepted: September 16, 2021
Published: October 7, 2021

Please cite this article in press as: Sidhik et al., High-phase purity two-dimensional perovskites with 17.3% efficiency enabled by interface engineering of hole transport layer, Cell Reports Physical Science (2021), https://doi.org/10.1016/j.xcrp.2021.100601

REFERENCES

1. Yoo, J.J., Seo, G., Chua, M.R., Park, T.G., Lu, Y., Rotermund, F., Kim, Y.-K., Moon, C.S., Jeon, N.J., Correa-Baena, J.-P., et al. (2021). Efficient perovskite solar cells via improved carrier management. Nature *590*, 587–593.
2. Ma, F., Zhao, Y., Li, J., Zhang, X., Gu, H., and You, J. (2021). Nickel oxide for inverted structure perovskite solar cells. J. Energy Chem *52*, 393–411.
3. You, J., Guo, F., Qiu, S., He, W., Wang, C., Liu, X., Xu, W., and Mai, Y. (2019). The fabrication of homogeneous perovskite films on non-wetting interfaces enabled by physical modification. J. Energy Chem. *38*, 192–198.
4. Tirado, J., Vásquez-Montoya, M., Roldán-Carmona, C., Ralaiarisoa, M., Koch, N., Nazeeruddin, M.K., and Jaramillo, F. (2019). Air-Stable n–i–p Planar Perovskite Solar Cells Using Nickel Oxide Nanocrystals as Sole Hole-Transporting Material. ACS Appl. Energy Mater. *2*, 4890–4899.
5. Di Girolamo, D., Di Giacomo, F., Matteocci, F., Marrani, A.G., Dini, D., and Abate, A. (2020). Progress, highlights and perspectives on NiO in perovskite photovoltaics. Chem. Sci. (Camb.) *11*, 7746–7759.
6. Saliba, M., Matsui, T., Seo, J.-Y., Domanski, K., Correa-Baena, J.-P., Nazeeruddin, M.K., Zakeeruddin, S.M., Tress, W., Abate, A., Hagfeldt, A., and Grätzel, M. (2016). Cesium-containing triple cation perovskite solar cells: improved stability, reproducibility and high efficiency. Energy Environ. Sci. *9*, 1989–1997.
7. Liu, Y., Akin, S., Pan, L., Uchida, R., Arora, N., Milić, J.V., Hinderhofer, A., Schreiber, F., Uhl, A.R., Zakeeruddin, S.M., et al. (2019). Ultrahydrophobic 3D/2D fluoroarene bilayer-based water-resistant perovskite solar cells with efficiencies exceeding 22. Sci. Adv. *5*, eaaw2543.
8. Zhang, S., Liu, Z., Zhang, W., Jiang, Z., Chen, W., Chen, R., Huang, Y., Yang, Z., Zhang, Y., and Han, L. (2020). Barrier Designs in Perovskite Solar Cells for Long-Term Stability. Adv. Energy Mater. *10*, 2001610.
9. Jang, Y.-W., Lee, S., Yeom, K.M., Jeong, K., Choi, K., Choi, M., and Noh, J.H. (2021). Intact 2D/3D halide junction perovskite solar cells via solid-phase in-plane growth. Nat. Energy *6*, 63–71.
10. Stoumpos, C.C., Cao, D.H., Clark, D.J., Young, J., Rondinelli, J.M., Jang, J.I., Hupp, J.T., and Kanatzidis, M.G. (2016). Ruddlesden–Popper hybrid lead iodide perovskite 2D homologous semiconductors. Chem. Mater. *28*, 2852–2867.
11. Ren, H., Yu, S., Chao, L., Xia, Y., Sun, Y., Zuo, S., Li, F., Niu, T., Yang, Y., and Ju, H. (2020). Efficient and stable Ruddlesden–Popper perovskite solar cell with tailored interlayer molecular interaction. Nat. Photonics *14*, 154–163.
12. Liang, C., Zhao, D., Li, Y., Li, X., Peng, S., Shao, G., and Xing, G. (2018). Ruddlesden–Popper perovskite for stable solar cells. Energy Environ. Mater. *1*, 221–231.
13. Tsai, H., Nie, W., Blancon, J.-C., Stoumpos, C.C., Asadpour, R., Harutyunyan, B., Neukirch, A.J., Verduzco, R., Crochet, J.J., Tretiak, S., et al. (2016). High-efficiency two-dimensional Ruddlesden-Popper perovskite solar cells. Nature *536*, 312–316.
14. Blancon, J.-C., Tsai, H., Nie, W., Stoumpos, C.C., Pedesseau, L., Katan, C., Kepenekian, M., Soe, C.M.M., Appavoo, K., Sfeir, M.Y., et al. (2017). Extremely efficient internal exciton dissociation through edge states in layered 2D perovskites. Science *355*, 1288–1292.
15. Zheng, K., and Pullerits, T. (2019). Two dimensions are better for perovskites. J. Phys. Chem. Lett. *10*, 5881–5885.
16. Quintero-Bermudez, R., Gold-Parker, A., Proppe, A.H., Munir, R., Yang, Z., Kelley, S.O., Amassian, A., Toney, M.F., and Sargent, E.H. (2018). Compositional and orientational control in metal halide perovskites of reduced dimensionality. Nat. Mater. *17*, 900–907.
17. Liu, L., Bai, Y., Zhang, X., Shang, Y., Wang, C., Wang, H., Zhu, C., Hu, C., Wu, J., Zhou, H., et al. (2020). Cation diffusion guides hybrid halide perovskite crystallization during the gel stage. Angew. Chem. Int. Ed. Engl. *59*, 5979–5987.
18. Chen, A.Z., and Choi, J.J. (2020). Crystallographic orientation and layer impurities in two-dimensional metal halide perovskite thin films. J. Vac. Sci. Technol. Vac. Surf. Films *38*, 010801.
19. Dong, Y., Lu, D., Xu, Z., Lai, H., and Liu, Y. (2020). 2-Thiopheneformamidinium-Based 2D Ruddlesden–Popper Perovskite Solar Cells with Efficiency of 16.72% and Negligible Hysteresis. Adv. Energy Mater. *10*, 2000694.
20. Huang, J., Wang, K.-X., Chang, J.-J., Jiang, Y.-Y., Xiao, Q.-S., and Li, Y. (2017). Improving the efficiency and stability of inverted perovskite solar cells with dopamine-copolymerized PEDOT: PSS as a hole extraction layer. J. Mater. Chem. A Mater. Energy Sustain. *5*, 13817–13822.
21. Tian, S., Chen, J., Lian, X., Wang, Y., Zhang, Y., Yang, W., Wu, G., Qiu, W., and Chen, H. (2019). Engineering the underlying surface to manipulate the growth of 2D perovskites for highly efficient solar cells. J. Mater. Chem. A Mater. Energy Sustain. *7*, 14027–14032.
22. Liao, Y., Liu, H., Zhou, W., Yang, D., Shang, Y., Shi, Z., Li, B., Jiang, X., Zhang, L., Quan, L.N., et al. (2017). Highly oriented low-dimensional tin halide perovskites with enhanced stability and photovoltaic performance. J. Am. Chem. Soc. *139*, 6693–6699.
23. Xu, Q., Meng, K., Liu, Z., Wang, X., Hu, Y., Qiao, Z., Li, S., Cheng, L., and Chen, G. (2019). Synergistic Improvements in Efficiency and Stability of 2D Perovskite Solar Cells with Metal Ion Doping. Adv. Mater. Interfaces *6*, 1901259.
24. Nie, W., Tsai, H., Blancon, J.-C., Liu, F., Stoumpos, C.C., Traore, B., Kepenekian, M., Durand, O., Katan, C., Tretiak, S., et al. (2018). Critical role of interface and crystallinity on the performance and photostability of perovskite solar cell on nickel oxide. Adv. Mater. *30*, 1703879.
25. Chia-Ching, W., and Cheng-Fu, Y. (2013). Investigation of the properties of nanostructured Li-doped NiO films using the modified spray pyrolysis method. Nanoscale Res. Lett. *8*, 33.
26. Wu, C.-C., and Shih, W.-C. (2017). Development of a highly transparent, low-resistance lithium-doped nickel oxide triple-layer film deposited by magnetron sputtering. Chem. Commun. (Camb.) *53*, 1634–1637.
27. Kotta, A., and Seo, H.K. (2020). Facile Synthesis of Highly Conductive Vanadium-Doped NiO Film for Transparent Conductive Oxide. Appl. Sci. (Basel) *10*, 5415.
28. Li, Y., Li, X., Wang, Z., Guo, H., and Li, T. (2016). One-step synthesis of Li-doped NiO as high-performance anode material for lithium ion batteries. Ceram. Int. *42*, 14565–14572.
29. Sharma, R., and Yadav, K. (2018). Effect of lattice defects on the structural and optical properties of Ni 1− X Ag XO (where X= 0.0, 0.01, 0.03, 0.05, 0.10 and 0.15) nanoparticles. Appl. Phys., A Mater. Sci. Process. *124*, 1–10.
30. Jiang, Y., Liu, B., Yang, W., Yang, L., Li, S., Liu, X., Zhang, X., Yang, R., and Jiang, X. (2017). Crystalline $(Ni_{1-x}Co_x)_5TiO_7$ nanostructures grown in situ on a flexible metal substrate used towards efficient CO oxidation. Nanoscale *9*, 11713–11719.
31. Habibi, M., Eslamian, M., Soltani-Kordshuli, F., and Zabihi, F. (2016). Controlled wetting/dewetting through substrate vibration-assisted spray coating (SVASC). J. Coat. Technol. Res. *13*, 211–225.
32. Kim, S.S., Heo, J.H., and Im, S.H. (2020). Wetting-induced formation of void-free metal halide perovskite films by green ultrasonic spray coating for large-area mesoscopic perovskite solar cells. RSC Advances *10*, 33651–33661.
33. Li, B., Chen, Y., Liang, Z., Gao, D., and Huang, W. (2015). Interfacial engineering by using self-assembled monolayer in mesoporous perovskite solar cell. RSC Advances *5*, 94290–94295.
34. Gu, Z., Zuo, L., Larsen-Olsen, T.T., Ye, T., Wu, G., Krebs, F.C., and Chen, H. (2015). Interfacial engineering of self-assembled monolayer modified semi-roll-to-roll planar heterojunction perovskite solar cells on flexible substrates. J. Mater. Chem. A Mater. Energy Sustain. *3*, 24254–24260.
35. Song, B., Hou, J., Wang, H., Sidhik, S., Miao, J., Gu, H., Zhang, H., Liu, S., Fakhraai, Z., and Even, J. (2020). Determination of Dielectric Functions and Exciton Oscillator Strength of Two-Dimensional Hybrid Perovskites. ACS Mater. Lett. *3*, 148–159.
36. Soe, C.M.M., Nagabhushana, G.P., Shivaramaiah, R., Tsai, H., Nie, W., Blancon, J.-C., Melkonyan, F., Cao, D.H., Traoré, B., Pedesseau, L., et al. (2019). Structural and thermodynamic limits of layer thickness in 2D halide perovskites. Proc. Natl. Acad. Sci. USA *116*, 58–66.
37. Sidhik, S., Li, W., Samani, M.H., Zhang, H., Wang, Y., Hoffman, J., Fehr, A.K., Wong, M., Katan, C., and Even, J. (2021). Memory seeds enable high structural phase purity in 2D

Please cite this article in press as: Sidhik et al., High-phase purity two-dimensional perovskites with 17.3% efficiency enabled by interface engineering of hole transport layer, Cell Reports Physical Science (2021), https://doi.org/10.1016/j.xcrp.2021.100601

perovskite films for high-efficiency devices. Adv. Mater. *33*, 2007176.

38. Kinigstein, E.D., Tsai, H., Nie, W., Blancon, J.-C., Yager, K.G., Appavoo, K., Even, J., Kanatzidis, M.G., Mohite, A.D., and Sfeir, M.Y. (2020). Edge States Drive Exciton Dissociation in Ruddlesden–Popper Lead Halide Perovskite Thin Films. ACS Mater. Lett. *2*, 1360–1367.

39. Kanemitsu, Y. (2017). Luminescence spectroscopy of lead-halide perovskites: materials properties and application as photovoltaic devices. J. Mater. Chem. C Mater. Opt. Electron. Devices *5*, 3427–3437.

40. Tavakoli, M.M., Waleed, A., Gu, L., Zhang, D., Tavakoli, R., Lei, B., Su, W., Fang, F., and Fan, Z. (2017). A non-catalytic vapor growth regime for organohalide perovskite nanowires using anodic aluminum oxide templates. Nanoscale *9*, 5828–5834.

41. Tavakoli, M.M., Dastjerdi, H.T., Prochowicz, D., Yadav, P., Tavakoli, R., Saliba, M., and Fan, Z. (2019). Highly efficient and stable inverted perovskite solar cells using down-shifting quantum dots as a light management layer and moisture-assisted film growth. J. Mater. Chem. A Mater. Energy Sustain. *7*, 14753–14760.

42. Liu, X., Rezaee, E., Shan, H., Xu, J., Zhang, Y., Feng, Y., Dai, J., Chen, Z.-K., Huang, W., and Xu, Z.-X. (2018). Dopant-free hole transport materials based on alkyl-substituted indacenodithiophene for planar perovskite solar cells. J. Mater. Chem. C Mater. Opt. Electron. Devices *6*, 4706–4713.

43. Liu, X., Tan, X., Chen, Q., Shan, H., Liu, C., Xu, J., Chen, Z.-K., Huang, W., and Xu, Z.-X. (2017). Facile synthesis of a dopant-free hole transporting material with a phenothiazine core for planar perovskite solar cells. RSC Advances *7*, 53604–53610.

44. He, Q., Yao, K., Wang, X., Xia, X., Leng, S., and Li, F. (2017). Room-temperature and solution-processable Cu-doped nickel oxide nanoparticles for efficient hole-transport layers of flexible large-area perovskite solar cells. ACS Appl. Mater. Interfaces *9*, 41887–41897.

45. Kim, H., Hong, J., Kim, C., Shin, E.-Y., Lee, M., Noh, Y.-Y., Park, B., and Hwang, I. (2018). Impact of hydroxyl groups boosting heterogeneous nucleation on perovskite grains and photovoltaic performances. J. Phys. Chem. C *122*, 16630–16638.

46. Liang, Z., Zhang, S., Xu, X., Wang, N., Wang, J., Wang, X., Bi, Z., Xu, G., Yuan, N., and Ding, J. (2015). A large grain size perovskite thin film with a dense structure for planar heterojunction solar cells via spray deposition under ambient conditions. RSC Advances *5*, 60562–60569.

47. Li, Y., Ding, B., Chu, Q.-Q., Yang, G.-J., Wang, M., Li, C.-X., and Li, C.-J. (2017). Ultra-high open-circuit voltage of perovskite solar cells induced by nucleation thermodynamics on rough substrates. Sci. Rep. *7*, 46141.

48. Li, X., Zhang, K., Li, J., Chen, J., Wu, Y., Liu, K., Song, J., and Zeng, H. (2018). Heterogeneous nucleation toward polar-solvent-free, fast, and one-pot synthesis of highly uniform perovskite quantum dots for wider color gamut display. Adv. Mater. Interfaces *5*, 1800010.

49. Pham, N.D., Tiong, V.T., Yao, D., Martens, W., Guerrero, A., Bisquert, J., and Wang, H. (2017). Guanidinium thiocyanate selective Ostwald ripening induced large grain for high performance perovskite solar cells. Nano Energy *41*, 476–487.

50. Chen, A.Z., Shiu, M., Ma, J.H., Alpert, M.R., Zhang, D., Foley, B.J., Smilgies, D.-M., Lee, S.-H., and Choi, J.J. (2018). Origin of vertical orientation in two-dimensional metal halide perovskites and its effect on photovoltaic performance. Nat. Commun. *9*, 1336.

51. Traore, B., Pedesseau, L., Blancon, J.-C., Tretiak, S., Mohite, A.D., Even, J., Katan, C., and Kepenekian, M. (2020). Importance of vacancies and doping in the hole-transporting nickel oxide interface with halide perovskites. ACS Appl. Mater. Interfaces *12*, 6633–6640.

Cell Reports Physical Science, Volume *2*

Supplemental information

High-phase purity two-dimensional perovskites with 17.3% efficiency enabled by interface engineering of hole transport layer

Siraj Sidhik, Yafei Wang, Wenbin Li, Hao Zhang, Xinjue Zhong, Ayush Agrawal, Ido Hadar, Ioannis Spanopoulos, Anamika Mishra, Boubacar Traoré, Mohammad H.K. Samani, Claudine Katan, Amanda B. Marciel, Jean-Christophe Blancon, Jacky Even, Antoine Kahn, Mercouri G. Kanatzidis, and Aditya D. Mohite

Supplemental Experimental Procedures

1. Methods and characterization

1.1 Thin-film fabrication

The 2D perovskite film fabrication technique involved two steps:

1) *$BA_2MA_3Pb_4I_{13}$ crystal-powder synthesis:* We synthesized the 2D Ruddlesden popper perovskite crystal powders of $BA_2MA_3Pb_4I_{13}$ by combining lead oxide (PbO, Sigma Aldrich, 99%), methylamine hydrochloride (MACl, Sigma Aldrich, ≥98%), and butylamine (BA, Sigma Aldrich, 99.5%) in appropriate ratios in a mixture of hydroiodic acid (HI, 57 wt% in H_2O) and hypophosphorous acid (H_3PO_2, 50% in H_2O). The solution was vigorously stirred and heated to a temperature of 220 ºC until it started boiling.The solution was then allowed to cool down at room temperature resulting in the crystallization of flat single crystals with a micrometer to millimeter size. The purity of the synthesized crystals was verified by X-ray diffraction and absorption measurements. Synthesized crystals with a purity of more than 90% were selected for film fabrication.

2) *$BA_2MA_3Pb_4I_{13}$ solution preparation and thin film fabrication:* To fabricate the thin films, we dissolved 0.4 M of the synthesized crystal-powders of $BA_2MA_3Pb_4I_{13}$ in N, N-Dimethylformamide (DMF, Sigma Aldrich, 99.999%) with an excess additive of 5.0 wt% MACl. The solution was aged at 70 ºC for almost 6 hrs. After cooling down, 100 µl of the solution was immediately spin-coated on the substrate at 4000 rpm for 30 sec followed by annealing at 100 ºC for 10 min.

1.2 Solar cell devices fabrication

We used an inverted planar architecture FTO/HTL/2D-perovskite-film/ETL/Ag for the solar cells. It combines nickel oxide (NiO_x) or lithium-doped nickel oxide (Li-doped NiO_X) as the HTL and PCBM as the ETL with a ~1 nm passivating layer of bathocuproine (BCP, Sigma Aldrich, 96%).

The top part of the solar cell comprised the patterned fluorine-doped tin oxide (FTO, Thin Film Device Inc.) substrates and the hole transporting layer (HTL). The FTO substrates were washed by ultrasonication in water, acetone, acetone/ethanol (50:50), and isopropyl alcohol for 15 min each. The substrates were further dried under nitrogen flow and treated with UV for 30 min. Then, a NiO_x or Li-doped NiO_X layer was spin-coated at 4000 revolutions per minute (r.p.m.) for 30 s, followed by three-step annealing at 150ºC for 10 min, 300ºC for 15 min, and 450ºC for 30 min (layer thickness was about 30 nm). The NiO_X solution was prepared by dissolving Nickel(II) acetate tetrahydrate (Sigma Aldrich, 99.995%) in absolute ethanol (Sigma Aldrich, 200 proof) with monoethanolamine (MEA, Sigma Aldrich, ≥99%). The ratio of Ni^{2+} and MEA was chosen to be 1:1. The NiO_X solution was stirred at 70 ^{o}C for 1 hour, while the Li-doped NiO_X solution was kept at 70 ºC under overnight stirring until a clear and deep green solution was obtained. The FTO/NiO_X or Li-doped NiO_X substrates were subsequently transferred to an argon-filled glovebox for the rest of the solar cell fabrication process.

Inside the glovebox, the 2D perovskite thin film (~250 nm) was deposited on the FTO/NiO_X or Li-doped NiO_X substrate as discussed in the thin film fabrication process above. After this, an electron transport layer, PCBM ($PC_{61}BM$, Sigma Aldrich, 99.9%) was deposited by spin-coating a 50 μl solution on the substrate at 1000 r.p.m for 45 s followed by annealing at 70 ºC for 10 min to form a thin film of ~30 nm. The PCBM solution was prepared by dissolving 25 mg PCBM in 1 ml of chlorobenzene, followed by overnight stirring at 60 ºC. Finally, the devices were evaporated with a 100 nm layer of silver using a shadow mask having an area of 3.14 mm^2.

1.3 Grazing incidence wide-angle x-ray scattering (GIWAXS)

Experimental methods: The FTO/NiO_X or Li-doped NiO_X/$BA_2MA_3Pb_4I_{13}$ thin-film high-resolution synchrotron patterns were measured at National Synchrotron Light Source-II (NSLS II) beamline 11-BM in Brookhaven National Lab. The RP *n*=4 perovskite thin-film was measured at the Advanced Photon Source (APS) beamline 8-ID-E at Argonne National Lab. At beamline 11-BM, samples were placed on a robotic stage inside a vacuum chamber (10^{-2} torr) with the sample 255 mm away from a Pilatus 800 K (Dectris) area detector. The photon energy was 13.5 keV, and the beam size was 200 μm × 50 μm (H × V).

GIWAXS analysis: The GIWAXS data were processed using the GIXSGUI package (version 1.7.3) running on Matlab 2018b (Mathworks) and using SciAnalysis in Visual Studio Code. All patterns were corrected with conditions such as detector sensitivity, X-ray polarization, and geometrical solid-angle parameters. The diffraction patterns were analyzed using the structural characteristics of 2D perovskite crystals reported in our previous work. The software SingleCrystal by CrystalMaker was used to simulate the x-ray diffraction of 2D perovskite crystals and assign Miller indices to diffraction peaks in the GIWAXS.

1.4 X-ray diffraction measurements

X-ray diffraction of crystals: The synthesized 2D perovskite crystals of $BA_2MA_3Pb_4I_{13}$ was characterized using powder X-Ray diffraction. The crystallized 2D perovskite powders were extracted immediately from the parent solution and dried using a Whatmann filter paper. The measurement was carried out for the 2θ between 2° and 15° with a step of 0.01° and a speed of 2 degrees per minute using a Rigaku SmartLab X-Ray diffractometer with Cu(K**α**) radiation ($\lambda = 1.5406$ Å). The corresponding Bragg peaks were identified and compared with the simulated diffraction obtained from the 2D perovskite structures discovered previously.[1,2] In case of the presence of impurities or mixed phases, the synthesized crystals were discarded, and the experiment was repeated until obtaining a parent-crystal powder with high phase purity (i.e. >90% of a single *n*-value).

X-ray diffraction of thin films: The x-ray diffraction of the thin films was measured for the 2θ between 2° and 32°, with a step of 0.01° and a speed of 2 degrees per minute, using a Rigaku SmartLab X-Ray diffractometer with Cu(K**α**) radiation ($\lambda = 1.5406$ Å).

1.5 Optical absorbance measurement

The thin film absorbance measurements were carried out by illuminating the samples using monochromatic light modulated at 2 kHz coming from a quartz-tungsten-halogen light source (SpectraPro HRS 300, Princeton instruments). The transmitted light was detected by a silicon photodiode connected to a SR865 lock-in amplifier.

1.6 Photoluminescence (PL) and time-resolved PL measurements

The PL and TRPL of the $BA_2MA_3Pb_4I_{13}$ 2D perovskite film deposited on NiOx and Li-doped NiOx surface were measured using a time-correlated single-photon counting (TCSPC) spectrophotometer (FS5 – Edinburgh Instruments). For PL, the samples were excited by a 405 nm laser, and the emission was collected at the range of 450-900 nm. For TRPL, the sample was excited by a 405 nm pulsed laser (repetition rate - 1 MHz), and the time-resolved emission was collected at the peak of the PL. The measured TRPL decay was fitted by a three-exponent function, convoluted with the instrument response function. The lifetime of each device was calculated based on a weighted average of the fitted decay.

1.7 Electronic band levels determination of pristine NiOx and Lithium-doped NiOx

Photoemission yield spectroscopy (AC-2, Riken-Keiki), was utilized to determine the valance band maximum (VBM) of the doped and undoped NiOx. The sample was illuminated by tunable monochromatic UV light under ambient conditions. A UV photon with higher energy than the ionization energy can ionize an electron into the vacuum level. This electron can ionize a gas molecule in proximity to the surface which is measured by the detector. For a typical measurement, the energy of the photons varies between 4.2 eV to 6.2 eV, and the number of generated photoelectrons is measured for each energy. This value is corrected according to the intensity spectrum of the UV lamp. For semiconductors, the number of photo-generated electrons near the VBM generally increases as a cube root of the energy. Hence the cube root of the corrected PYSA spectrum is plotted against the photon energy. The linear region of the plot above the onset is fitted to find the VBM, at the crossing of the linear fit and the background level. The conduction band minimum (CBM) with respect to the vacuum level (electron affinity (EA)), is calculated by subtracting the measured bandgap from the ionization energy.

1.8 Ultraviolet photoemission spectroscopy (UPS) and inverse photoemission spectroscopy (IPES) measurements

UPS and IPES were performed in ultrahigh vacuum (10^{-10} torr) at room temperature. The 2D perovskite samples were transferred without ambient exposure. The work function and valence band edges were measured in UPS using He I (21.22 eV) photons generated by a discharged lamp. Valence band spectra were recorded and plotted on a logarithmic intensity scale due to the low density of states near the band edge. The conduction band edge energetic position (electron affinity) was measured in IPES in the sample chamber, in the isochromat mode, with electron energies of 5–15 eV onto the sample. The Fermi level reference for both UPS and IPES were determined on a clean Au surface.

1.9 Extraction of phase purity using simulated absorption

The simulated absorption spectrum of a uniform thin film can be estimated based on Beer-Lambert law using the measured absorption coefficient reported by Deep *et al.*,.[3] Neglecting light scattering, the amount of light attenuation is described:

$$T(\lambda) = \frac{I_T}{I_0} = \exp(-\alpha(\lambda)\, d) \qquad (1)$$

where $T(\lambda)$ is the light transmittance, d is the thickness of film and $\alpha(\lambda)$ is the absorption coefficient of the material.

For a perovskite film with phase impurity, the mean absorption coefficient $\alpha(\lambda)$ can be estimated by the ensemble average of multiple phases. Assuming the uniform spatial distribution of each phase, the absorption coefficient is calculated by:

$$\alpha(\lambda) = \sum_i n_i \alpha_i(\lambda) \qquad (2)$$

Here $\alpha_i(\lambda)$ stands for the absorption coefficient of each perovskite phase (n=1, 2,…5) and n_i is the percentage of the corresponding phase. For perovskite films with n≥3, additional absorbance rises from the edge stage absorption starting at ~750nm, which is not observed in single crystal absorption[4]. Therefore, an additional linear slope is added to simulate edge state absorption

$$\alpha_{edge}(\lambda) = k(\lambda_0 - \lambda),\ \lambda < \lambda_0 \tag{3}$$

Where k is the slope of absorption and $\lambda_0$is the starting point (intercept). Therefore, the total absorption coefficient is estimated by:

$$\alpha(\lambda) = \sum_i n_i \alpha_i(\lambda) + k(\lambda_0 - \lambda) \tag{4}$$

1.10 Solar cell devices characterization

Solar cell performances: The performances of the fabricated solar cells were characterized by measuring the current-voltage (J-V) curves of each device illuminated by an ABB solar simulator from Newport (model 94011). The arc simulator modeled AM 1.5G irradiance of 100 mW/cm^2 whose intensity was calibrated using a NIST-certified Si solar cell (Newport 91150V, ISO 17025). and corrected by measuring the spectral mismatch between the solar spectrum, reference cell, and the spectral response of the PV device. We estimate a mismatch factor of 3%. The solar cells were measured with a Keithley 2401 instrument from 1.2 to 0 V and back, with a step size of 0.05 V and a dwell time of 0.1 s, after light soaking for 10 s. The active area was defined using the was 3.14 mm^2.

External quantum efficiency: The external quantum efficiency of the solar cell devices was collected by first illuminating each device with monochromatic light modulated at 2 kHz coming from a quartz-tungsten-halogen light source fed into a monochromator (SpectraPro HRS 300, Princeton instruments). The photocurrent response of the solar cells was measured by a SR865 lock-in amplifier. The light source spectrum response was calibrated using a calibrated silicon diode (FDS1010, Thorlab).

Stability tests: For stability test measurements, the 2D perovskite devices were encapsulated with a UV- curable epoxy (Poland Inc.) and a glass coverslip as a barrier layer in an argon-filled glove box. The devices were blown with the argon gun in order to remove any contaminants or dust particles just before encapsulation. All the devices were tested at the continuos maximum power point condition, under full-spectrum simulated AM 1.5G (100 mA cm^{-2} irradiance) in air using an ABB solar simulator (94011A, Newport) – ISOS-L protocol. Each data point was collected after an interval of 15 min. The relative humidity was measured to be constant at 60 ± 5 %RH.

Supplemental References

1. Stoumpos, C.C., Cao, D.H., Clark, D.J., Young, J., Rondinelli, J.M., Jang, J.I., Hupp, J.T., and Kanatzidis, M.G. (2016). Ruddlesden–Popper hybrid lead iodide perovskite 2D homologous semiconductors. Chem. Mater. *28*, 2852–2867.
2. Mao, L., Ke, W., Pedesseau, L., Wu, Y., Katan, C., Even, J., Wasielewski, M.R., Stoumpos, C.C., and Kanatzidis, M.G. (2018). Hybrid Dion–Jacobson 2D lead iodide perovskites. J. Am. Chem. Soc. *140*, 3775–3783.
3. Song, B., Hou, J., Wang, H., Sidhik, S., Miao, J., Gu, H., Zhang, H., Liu, S., Fakhraai, Z., Even, J., et al. (2021). Determination of Dielectric Functions and Exciton Oscillator Strength of Two-Dimensional Hybrid Perovskites. ACS Mater. Lett. *3*, 148–159.
4. Blancon, J.-C., Tsai, H., Nie, W., Stoumpos, C.C., Pedesseau, L., Katan, C., Kepenekian, M., Soe, C.M.M., Appavoo, K., Sfeir, M.Y., et al. (2017). Extremely efficient internal exciton dissociation through edge states in layered 2D perovskites. Science *355*, 1288–1292.

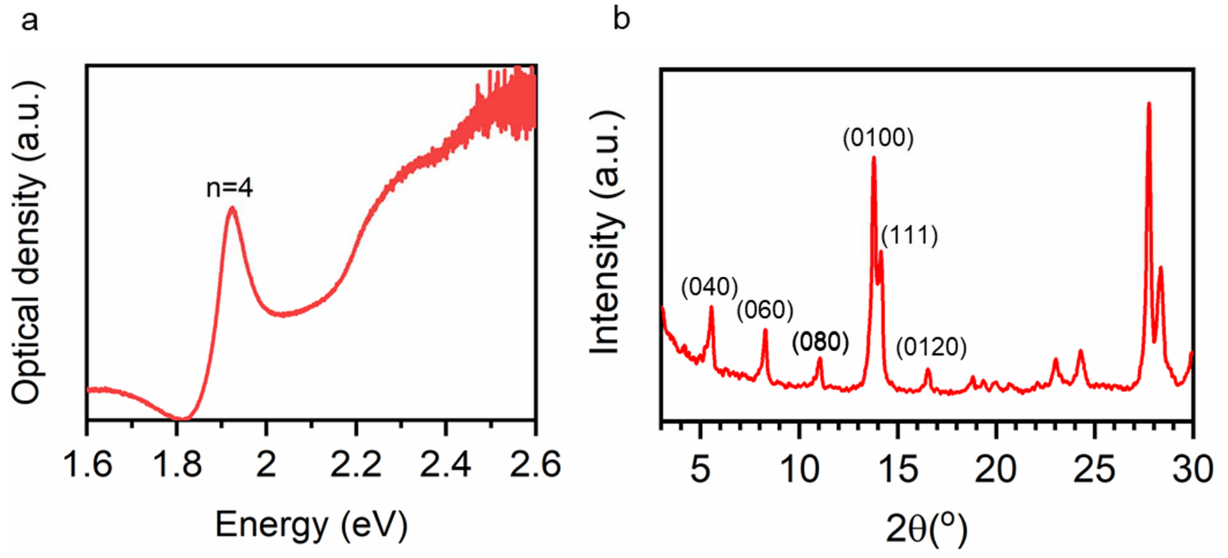

Figure S1. Optical characterization of $BA_2MA_3Pb_4I_{13}$ 2D perovskite crystal powders. a) Absorption spectra of the synthesized $BA_2MA_3Pb_4I_{13}$ 2D perovskite crystals with a strong excitonic peak absorption, b) powder x-ray diffraction of the synthesized $BA_2MA_3Pb_4I_{13}$ 2D perovskite crystal powders indicating the right *n* thickness verified by the low angle diffraction peaks.

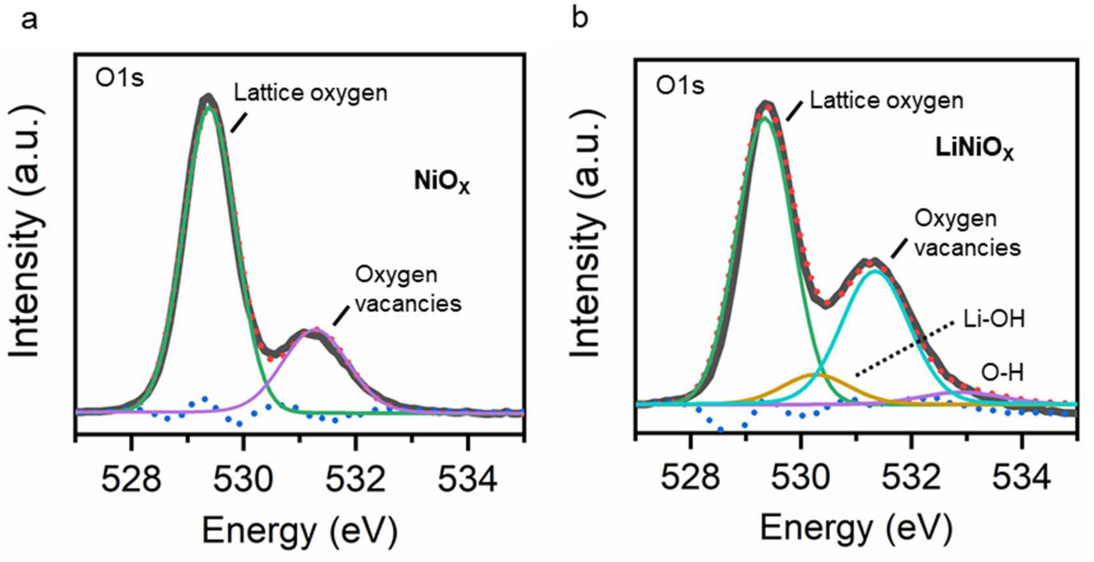

Figure S2. Surface analysis of the nickel oxide film. Deconvoluted O 1s spectra of the pristine NiO_X and the Li-doped NiO_X film indicating the presence of lithium intercalated within the nickel oxide lattice. The dotted red line indicates the fitted O1s spectra and the dotted blue line denotes the residual spectra.

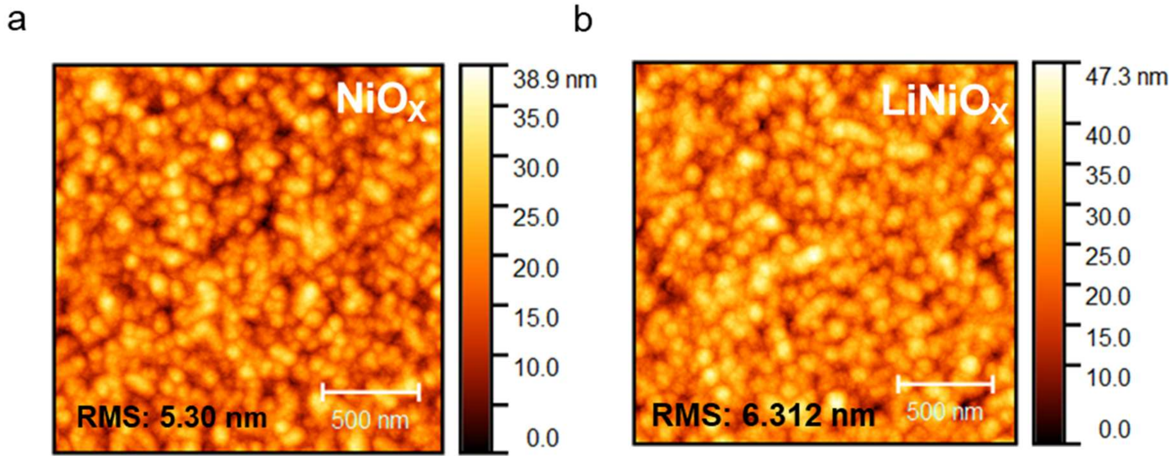

Figure S3. Morphology of the nickel oxide hole transport layer. a) Morphology of the pristine NiOx and Li-doped NiOx with the extracted root-mean-square roughness obtained by atomic force microscopy.

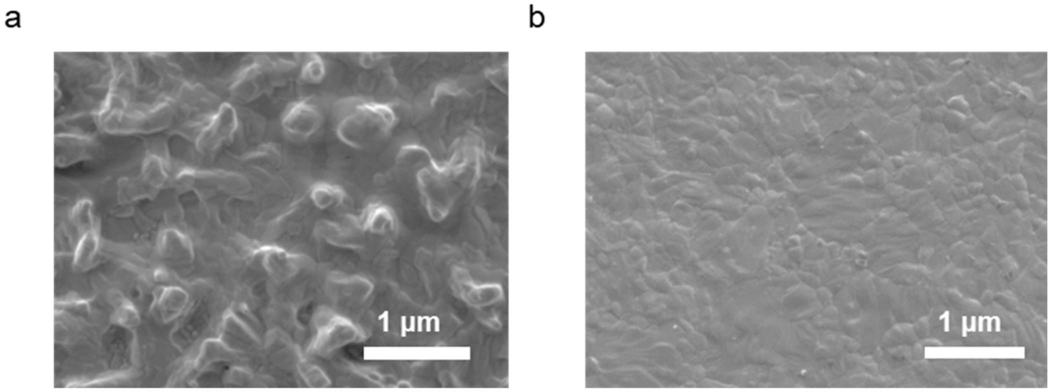

Figure S4. Surface morphology of the 2D perovskite film. Morphology of the $BA_2MA_3Pb_4I_{13}$ 2D perovskite film grown on top of the **a)** pristine NiOx and, **b)** Li-doped NiOx (10%) measured using scanning electron microscopy.

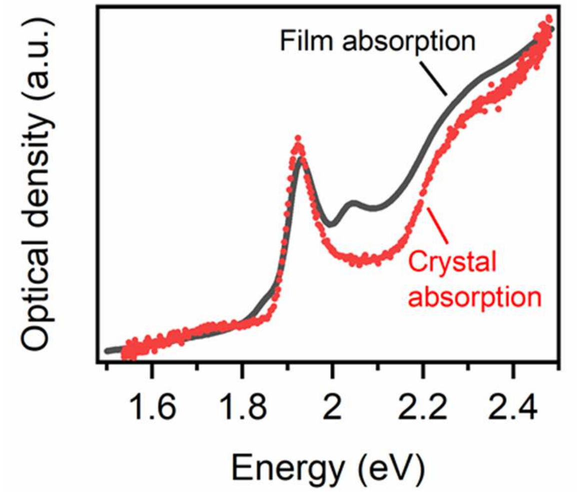

Figure S5. Direct comparison with the 2D perovskite crystals. Absorption spectra of the $BA_2MA_3Pb_4I_{13}$ 2D perovskite film grown on top of Li-doped NiOx, and comparing it to the crystal absorption.

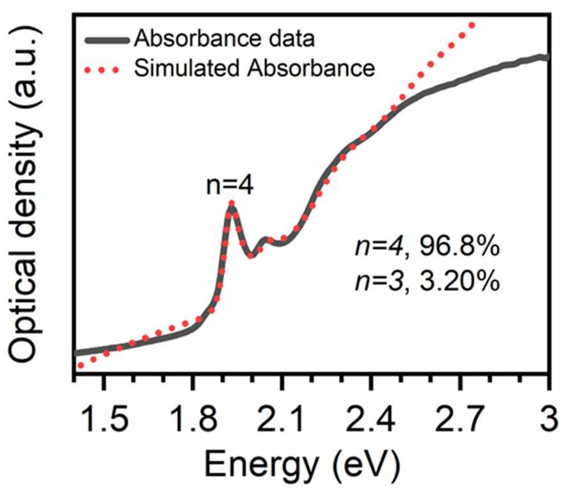

Figure S6. Evaluation of the phase purity of 2D perovskite thin film. Absorption spectra of the $BA_2MA_3Pb_4I_{13}$ 2D perovskite film grown on top of Li-doped NiOx, and comparing it to the simulated absorbance considering the absorption coefficient of *n=3*, and *n=4* Ruddlesden-popper 2D perovskite.

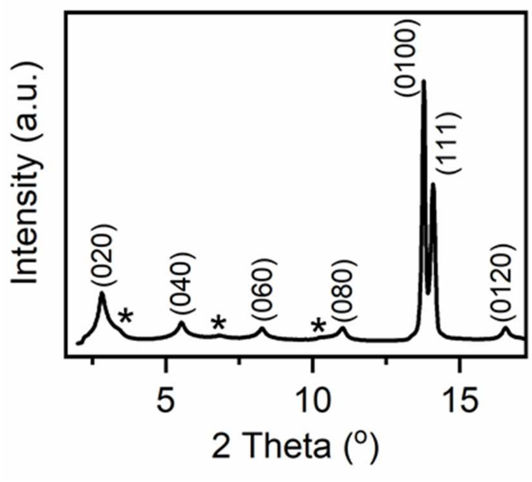

Figure S7. Phase purity examined by powder X-ray diffraction. Plots showing the a. powder X-ray diffraction of the scratched powder obtained from the oriented $BA_2MA_3Pb_4I_{13}$ 2D perovskite films. The symbol star denotes the n=3 phase impurity in the $BA_2MA_3Pb_4I_{13}$ 2D perovskite films.

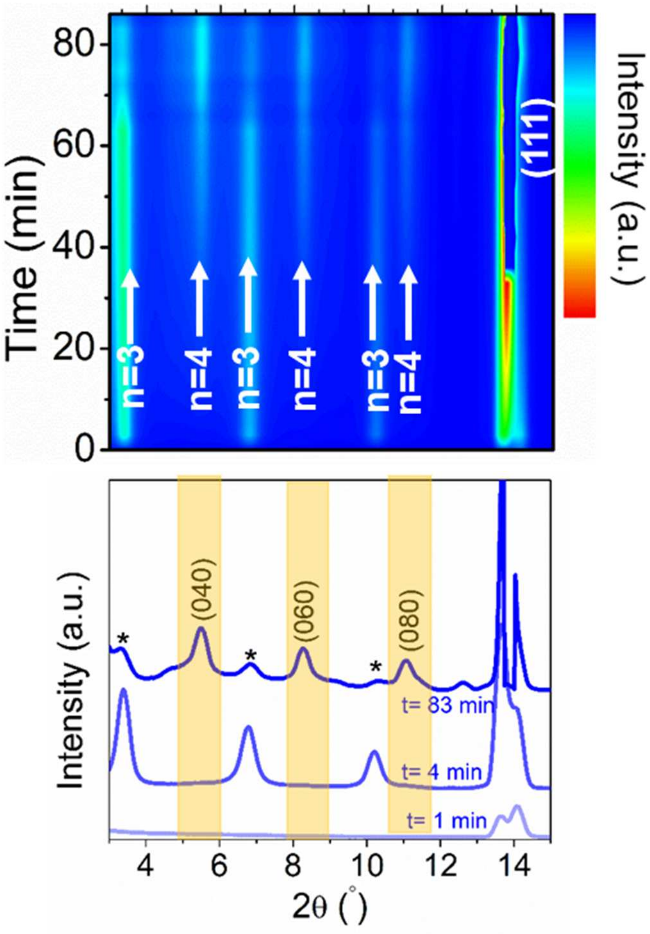

Figure S8. In-situ X-ray diffraction for the 2D perovskite film growth. Evolution of the x-ray diffraction of the $BA_2MA_3Pb_4I_{13}$ 2D perovskite film as a function of time. All peaks were identified to a 2D perovskite phase of defined *n*-value (or perovskite layer thickness).

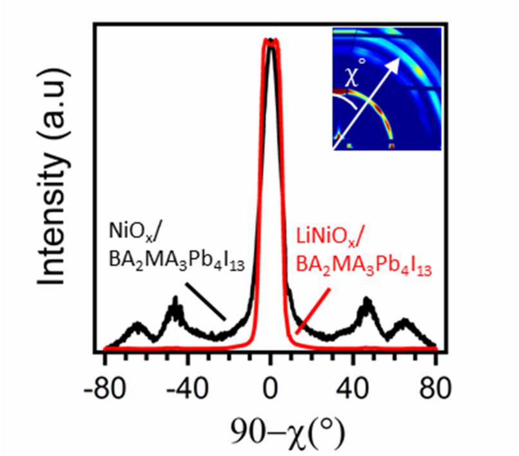

Figure S9. Orientation of 2D perovskite film extracted from the GIWAXS measurements Chi-plot showing the azimuthal angular profile of the (111) diffraction peak of the $BA_2MA_3Pb_4I_{13}$ film fabricated on the two nickel oxide surfaces, depicting the orientation of the crystallite domains.

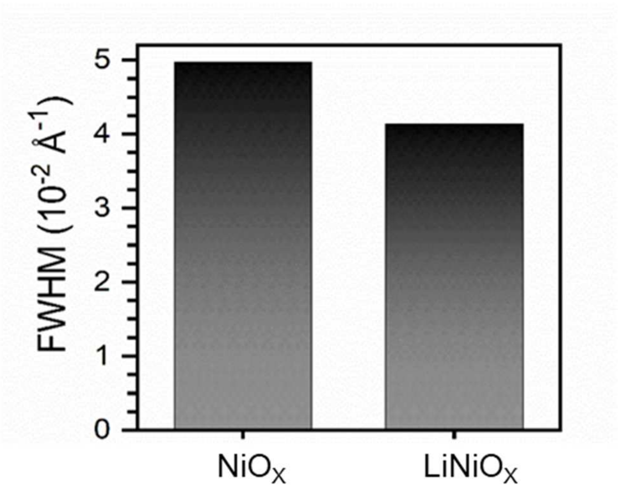

Figure S10. Crystallinity of the 2D perovskite film extracted from the GIWAXS measurements. Full width at half maximum (FWHM) evaluated from the angular integration of the GIWAXS patterns of $BA_2MA_3Pb_4I_{10}$ films fabricated on top of the pristine NiOx and Li-doped NiOx.

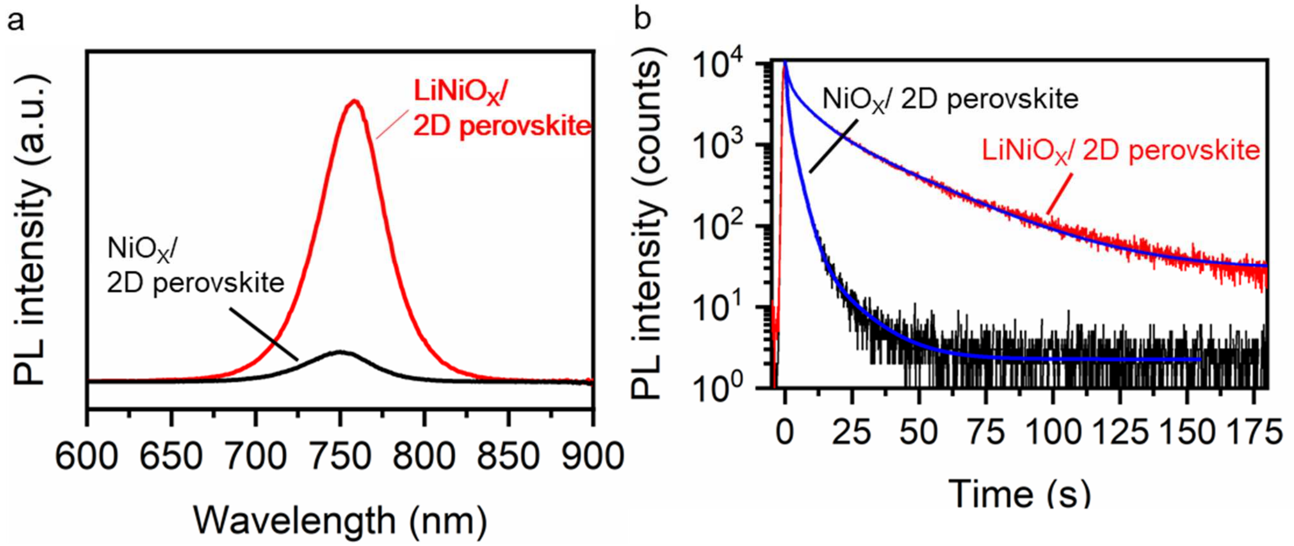

Figure S11. Charge carrier dynamics of 2D perovskite thin films. a) Photoluminescence measurement of the 2D perovskite film grown on the two nickel oxide surfaces to evaluate the recombination phenomenon. b) The time-resolved photoluminescence spectra of the 2D perovskite film grown on top of the two nickel oxide surfaces to extract the charge carrier lifetime indicating the change in recombination.

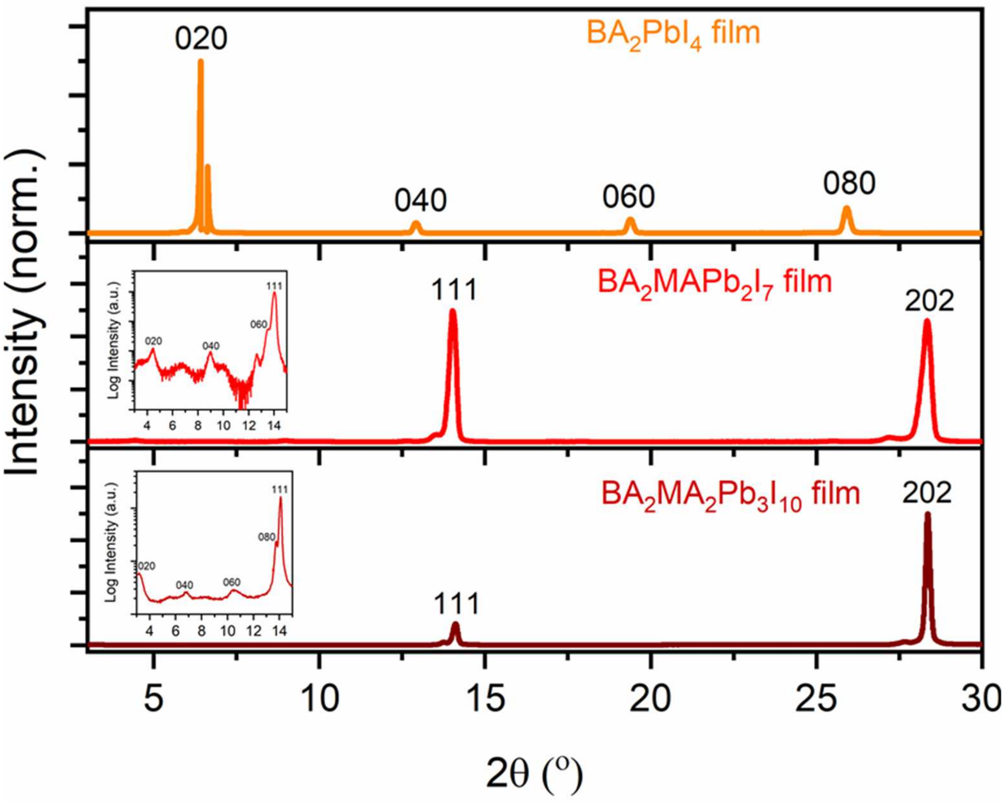

Figure S12. Orientation of the lower *n* 2D perovskite thin films. X-ray diffraction of the 2D perovskite films (n<4) grown on top of Li-doped NiO_X showing preferential orientation in vertical direction.

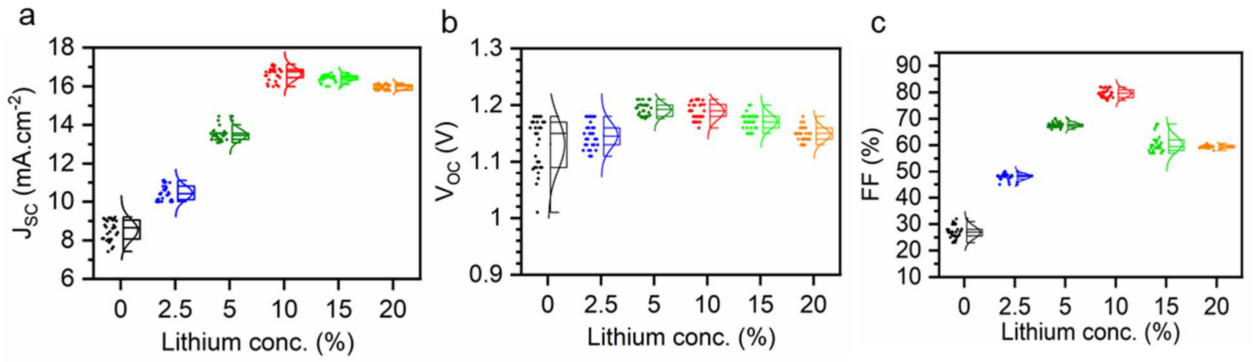

Figure S13. Solar cell performance of 2D perovskite devices. a-c) Statistics of the photovoltaic parameters of $BA_2MA_3Pb_4I_{13}$ 2D perovskite solar cells fabricated on top of NiOx HTL with different doping concentration of Li.

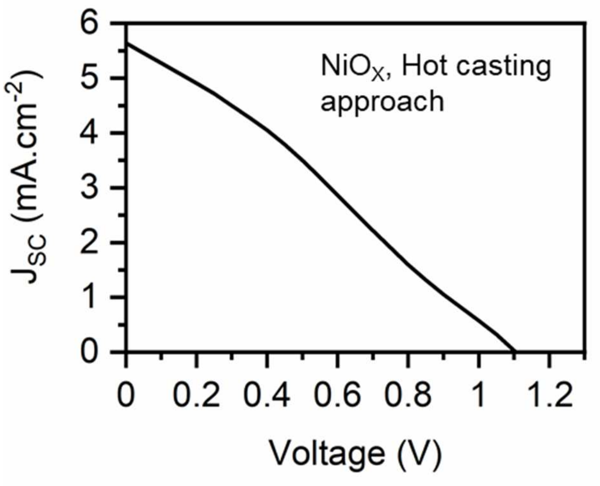

Figure S14. Solar cell characteristics of Hot casting approach. Current-voltage characteristics of the of $BA_2MA_3Pb_4I_{13}$ 2D perovskite solar cell fabricated on pristine NiOx using hot casting approach.

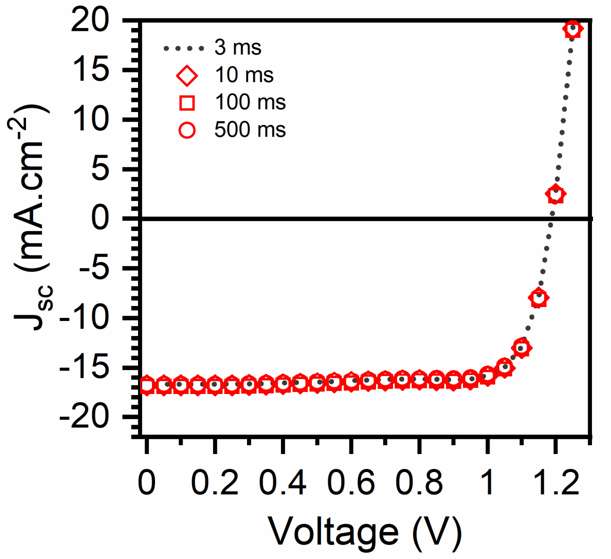

Figure S15. Hysteresis behavior of 2D perovskite solar cells. Current-voltage characteristics of the $BA_2MA_3Pb_4I_{13}$ 2D perovskite solar cell fabricated on Li-doped NiOx (10%) measured at different scan speeds.

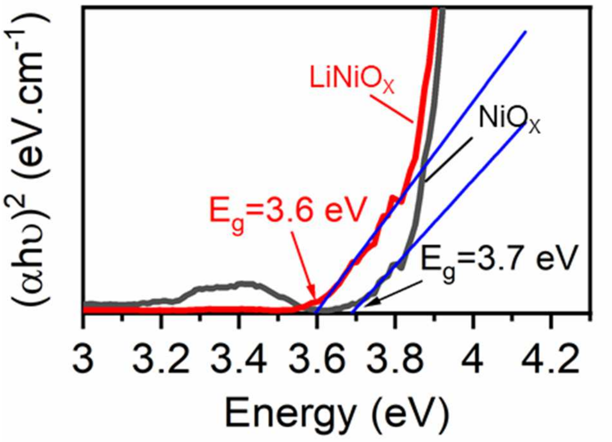

Figure S16. Bandgap measurement of nickel oxide HTL. Tauc plot showing the change in the bandgap of the pristine NiO_X and Li-doped NiO_X.

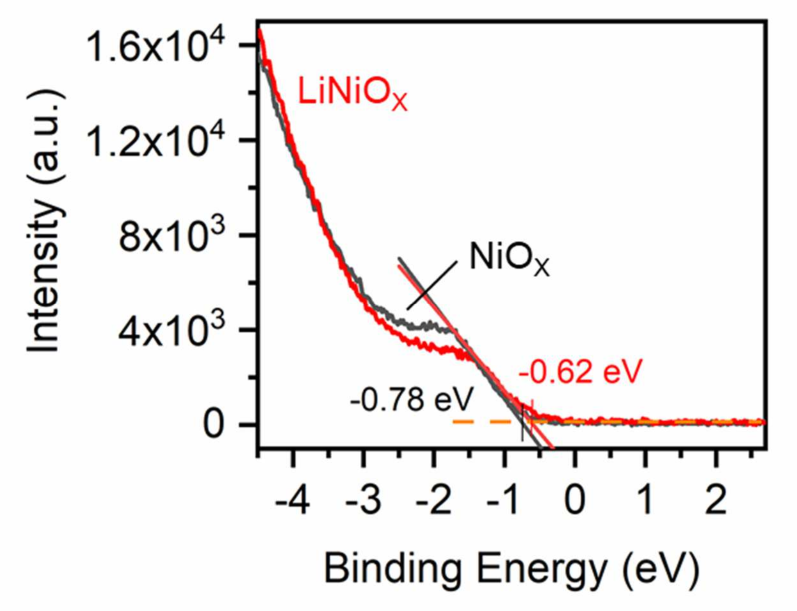

Figure S17. Band levels of nickel oxide HTL. The UPS spectra of the pristine NiO_X and Li-doped NiO_X showing the energy difference between the valence band maximum and the fermi level.

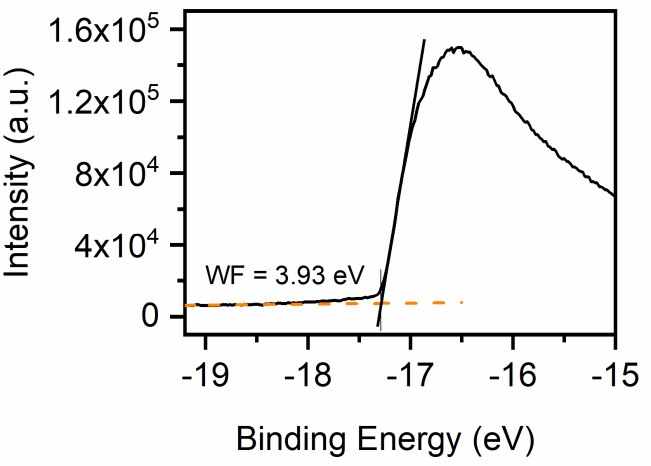

Figure S18. Work function of 2D perovskite film. The UPS spectra of the $BA_2MA_3Pb_4I_{13}$ 2D perovskite film showing the extracted work function.

Table S1. TRPL tri-exponential fitting parameters. The fitted parameters of the tri-exponential fit of the TRPL decay showing the lifetime of the edge states for the $BA_2MA_3Pb_4I_{13}$ 2D perovskite films deposited on NiO_X and Li-doped NiO_X.

Samples	A_1	τ_1 (ns)	A_2	τ_2 (ns)	A_3	τ_3 (ns)
NiO_X/ $BA_2MA_3Pb_4I_{13}$	7295.45	0.613	3043.13	2.861	72.79	12.17
Li-doped NiO_X/ $BA_2MA_3Pb_4I_{13}$	4422.76	1.1	2429.48	7.94	3443.63	21.08

Table S2. TRPL bi-exponential fitting parameters. The fitted parameters of the bi-exponential fit of the TRPL decay from the bulk of the $BA_2MA_3Pb_4I_{13}$ 2D perovskite films deposited on NiO_X and Li-doped NiO_X.

Samples	A_1	τ_1	A_2	τ_2
NiO_X/ $BA_2MA_3Pb_4I_{13}$	13318.63	1.3	7872.94	16.29
Li-doped NiO_X/ $BA_2MA_3Pb_4I_{13}$	15937.09	0.9	3692.37	6.79